

BAINITIC KINETICS

BAINITIC KINETICS

by

John Berwick Tiley, B. Eng.

A Thesis

Submitted to the School of Graduate Studies

In Partial Fulfillment of the Requirements

for the Degree

Master of Engineering

McMaster University

September 1972

Master of Engineering (1972)
(Metallurgy)


McMaster University
Hamilton, Ontario

Title: Bainitic Kinetics

Author: John Berwick Tiley, B. Eng. (McMaster University)

Supervisor: Professor G. R. Purdy

Number of Pages: 66



ACKNOWLEDGEMENTS

The author gratefully thanks his supervisor, Dr. G. R. Purdy, for suggesting the topic of this research and for his inspiration, guidance, understanding and patience during the course of this study. As well, a special thankyou to Messrs. I. Jin and D. Stephens, fellow students, for many discussions which helped the author to a greater understanding of the fundamental concepts involved in this field. Thanks also to the faculty, technical staff and graduate students of the Department of Metallurgy and Materials Science for their most helpful advice and assistance.

The financial support of the Department of Metallurgy (in the form of a teaching assistantship) and the National Research Council of Canada (in the form of research grants to Dr. Purdy) are gratefully acknowledged.

ABSTRACT

The growth kinetics of α plates and rods in β -brass have been calculated using a local equilibrium model. These are in good agreement with published experimental data. Along with this, quantitative microanalysis of deep etched specimens is cited in support of the proposed diffusional mechanism for their formation.

The model was also employed to calculate the growth rates of upper bainitic rods in the Fe-C-Ni system at 400° C. A "phase diagram" was constructed in order to supply the effective supersaturations required by the local equilibrium model. Lengthening rates were also calculated using a paraequilibrium interface condition. The experimental data were correctly predicted assuming the former case but failed at the "phase" boundary. It seems that a solute drag might well operate in this system. These results have provided some further indication of the part alloying elements play in the formation of the microstructural constituents of steel.

TABLE OF CONTENTS

	PAGE NO.
INTRODUCTION	1
PART I	
The Copper-Zinc System	
I - Introduction	5
II - Theory	8
III - Experimental	
(a) preparation of material	11
(b) procedure	11
IV - Results	13
PART II	
Bainitic Steels	
I - Introduction	16
II - Theory - (a) calculation of the Fe-C-Ni isotherm	18
(b) kinetic calculations	21
III - Experimental	22
IV - Results	23
DISCUSSION	24
SUMMARY	
CONCLUSIONS	29
APPENDIX I	30
REFERENCES	32

LIST OF FIGURES AND TABLES

- TABLE I (a) Calculation data for Fe-C-Ni system.
(b) Calculation data for Cu-Zn system.
- FIG. I - A portion of the Cu-Zn Equilibrium diagram.
- FIG. II - Comparison of calculated and published experimental growth rates of α plates and rods in β -brass.
- FIG. III - Sample microprobe scan across α plates and rods in β -brass.
- TABLE II (a) Summary of microprobe analysis of α brass plates (40.3 wt.% Zn - 250° C)
(b) Summary of X-ray fluorescence spot analysis of α brass plates (40.3 wt.% Zn - 250° C)
- FIG. IV - A portion of the Fe-C Equilibrium diagram.
- FIG. V - (a) and (b) - TTT curves for Fe-C-Ni system iron rich region.
- Fig. VI - Schematic representation of paraequilibrium diagram for Fe-C-Ni system Fe-rich corner (400° C)
- FIG. VII - Schematic free energy surfaces for ferrite and austenite illustrating paraequilibrium conditions.
- FIG. VIII - The effect of the no partition region on the distribution of nickel between ferrite and austenite assuming local equilibrium.
- FIG. IX - The effect of thermodynamic interaction on the no partition phase field.
- FIG. X - The effect of growth rate on the solute concentration profile assuming a boundary drag is in force.

- FIG. XI - Calculated Fe-rich corner of the Fe-C-Ni system at 400° C.
- FIG. XII - Geometry of the Fe-C-Ni phase diagram used to calculate the envelope of zero partition.
- FIG. XIII - Comparison of calculated local equilibrium no partition and paraequilibrium growth rates with experimental values
- FIG. XIV - Example of computer outplot of velocity vs. peclet number for plates at 250°Cu(42.5% Zn)
- FIG. XV - Example of computer outplot of critical radius ratio vs peclet number for plates at 250° Cu(42.5% Zn)

LIST OF MICROGRAPHS

(A)	Cu 40.3 wt.% Zn 250°C	MAG.
I 1	α plate plane view	1500
I 2	Same plate view of sideways growth	6800
I 3	Same plate view of faceting	1300
I 4	Two α plates plane view	1200
I 5	Tip of thin α plate	3000
I 6	Tip of thin α plates - 3 faces	6500
I 7	Group of coarsely faceted α precipitates	2000
I 8	Closeup of same precipitates	10000
I 9	Orientation relationship of α precipitate growth	3000
I 10	Plane view of sheave of α needles	1300
I 11	Closeup of tip from same sheave	3300
I 12	Cross-section of sheave of needles	3300
I 13	Face of α plate showing midrib	6000
I 14	Opposite face of similar α plate	6700
I 15	General group of α precipitates including grain boundary	1350
I 16	Group of α plates	2200
I 17	Group of α plates	1300

(B) Fe-C-Ni System 400^o C Upper Bainite Rods x 1100

J I	Fe -.8% C	2 % Ni
J II	Fe -.2% C	2 % Ni
J III	Fe - 1% C	5% Ni
J IV	Fe - 1% C	4% Ni
J V	Fe -.2% C	4% Ni
J VI	Fe - .8% C	4% Ni

INTRODUCTION

In 1930 Davenport and Bain⁽¹⁾ succeeded in producing, by isothermal treatments, a structure intermediate between the equilibrium constituents of steel and martensite^(Fig. 4). This 'bainite' consists of an aggregate of acicular ferrite and carbides. Its morphology changes progressively with the transformation temperature in that the size and distribution of the particles and the acicularity of the structure increase as the temperature decreases. The reaction is unusual in that it exhibits features common to both diffusion-controlled and martensitic transformations. Analogous decompositions are also found to occur on non-ferrous systems involving only substitutional components⁽²⁾.

The complexity of the microstructural, kinetic, and surface relief features has made it difficult to decide on the reaction mechanism or the specific processes controlling the reaction rate. Recently Aaronson⁽³⁾ has outlined these approaches toward the description of the formation while discussing their mutual incompatibility:

- (a) The microstructural definition - a eutectoid reaction in which the product is formed by the precipitation of a non-lamellar dispersion of carbides in association with pro-eutectoid ferrite.
- (b) The kinetic definition - the bainite reaction has its own C-curve lying below that of pearlite^(Fig. 5). This becomes more evident during the presence of alloying elements. It forms when supersaturated ferrite

grows under diffusional rate control followed by carbide precipitation.

(c) The surface relief definition - this presumes a martensitic interface motion that is controlled by the diffusion of interstitial carbon; which behaves independently during the shearing of the iron matrix. The result is a compositional change.

Some of the confusion associated with bainite formation lies in the fact that the bainitic transformation can be divided into two parts according to the microstructural aspects of the product. As the temperature of the system is lowered below the pearlite nose and the free energy change driving the f.c.c. to b.c.c. structure increases, ferrite plays an increasingly predominant part in the transformation. The pro-eutectoid ferrite and ferrite + cementite curves in the TTT diagram run together and the transformation is nucleated by the formation of Widmanstätten plates of ferrite. Only the acicular ferrite can grow at appreciable rates owing to the slow diffusion of carbon. Since the plates reject carbon as they grow, the austenite left behind them is enriched in carbon. As a result, carbides nucleate and grow in the regions parallel to the plates. The final structure is referred to as upper bainite. As the temperature is decreased, the plates become finer and show up as only a feathery constituent in optical micrographs. At still lower temperatures, the plates form separately and in a variety of well-defined crystallographic directions. In these plates, carbides form within the ferrite matrix at an angle to the growth axis. This structure is referred to as lower bainite.

Isothermal growth rates of upper bainite in plain carbon steels conform approximately to a volume-diffusion-control model using the best available diffusion data and extrapolated phase equilibria⁽⁴⁾. However, Hehemann⁽²⁾ claims that the observed retardation effects of alloying elements cannot be explained using this approach. Hence he argues that the bainite initially inherits the full carbon content of the austenite and rejects it as time goes on. Kinsman, however, has demonstrated by microprobe analysis that bainitic ferrite has a low carbon content⁽⁵⁾.

In order to analyse the observed kinetics, this investigation will use a refined local equilibrium model to calculate the lengthening of a bainitic plate in the Fe-C-Ni system at 400° C. Phase equilibria will be obtained from a theoretical calculation of the Iron-rich corner of the ternary field. The solution to the growth rate of a paraboloid of revolution will include the effects of non-ideality involved in the alloy element interaction parameters.

In order to study the applicability of a growth model to ternary systems, it is often convenient to choose a binary system exhibiting the same type of crystallography and morphology. The β to α brass transformation occurs isothermally as both rod and plate shaped products at temperatures considerably above the subzero M_s temperature. The rods have a general Widmanstätten nature while the plates are considered "bainitic" (but note the prior restrictions about the definition of bainites).

Although both exhibit C-curve kinetics, the published crystallography, microcompositional, and kinetic data are contradictory in the case of the plates. These are internally faulted⁽⁶⁾ and possess midribs⁽⁷⁾. The predominant viewpoint is that no long-range diffusion is involved in their growth^(8, 9, 15). This was supported by the microprobe work of Flewitt and Towner⁽⁸⁾, and by the lengthening rate measurements of Repas and Hehemann,⁽⁹⁾ which were thought to be much in excess of that required for volume diffusion control. These results led to a proposal for a shearing mechanism as the rate controlling factor in their formation.

This investigation aims to re-interpret their experimental results using the model described in the above which exists as a result of Trevedi's kinetic calculations⁽¹⁰⁾. Along with this, a new deep-etching technique will be used to isolate the α plate tip and allow quantitative microprobe analysis without interference from the surrounding matrix. These results will be used in support of a diffusionaly regulated mechanism for the lengthening rate of the α plates in this transformation. The ternary system will then be treated as a special case of the binary solution. From a comparison of the experimental results with various ternary equilibria, it is hoped that new insight may be gained into the role of alloying elements in steels.

PART I

The Copper-Zinc System

I Introduction

A portion of the copper-zinc binary phase diagram is shown in Figure 1. On cooling 100% β alloys of roughly 40-45% Zn there is a precipitation similar to that of ferrite from austenite. A study of the orientation relationship between the b.c.c. β Matrix and the f.c.c. α precipitate indicates that the close packed planes and directions of the two phases are approximately parallel. Also, the morphology of the microstructures produced obeys similar T.T.T. curves⁽⁸⁾ to those found in the Fe-C system. However, this is a substitutional rather than an interstitial solution system. As well, there is an order-disorder transition at 450° C which has a pronounced thermodynamic effect on the transformation kinetics. Within the temperature range 500-200° C, the needle-to-plate transition occurs. There have been observations of both internally⁽⁷⁾ as well as surface⁽¹¹⁾ nucleated needles and plates. But the true shape of the bulk precipitates can be unambiguously determined from studies of surface formations because of the markedly different conditions for growth involved.

The crystallography of the transformation (both plate and needle like) has been established in a number of investigations⁽¹²⁾. The needles exhibit approximately a Kurdjumov-Sachs orientation relationship;

$(011)_\beta$ b.c.c. // to $(111)_\alpha$ f.c.c. compatible with their Widmanstätten nature. These have the equilibrium f.c.c. structure. There is a shape change revealed by interferometry but there is no detectable displacement of previously introduced slip lines⁽¹¹⁾. In general the rods exhibit a roof-gable relief and display habits which are variants of irrational directions near (111). Although these observations suggest a shearing mechanism for rod formation, volume diffusion of Cu and Zn appears to be involved. The plates nucleate in clusters and often occur as V-pairs generally separated by an obtuse angle of 166° . However, a limited number of acute-angle pairs are also seen which is a characteristic of the sub-zero martensite of this system. Also closed loops consisting essentially of eight sections are observed. The habit plane is $\{2\ 11\ 12\}$ near $\{0\ 11\}$ or the four associated variants. This is also characteristic of the martensite, as is their invariant plane strain relief effect. The pair grows from a common $\{100\}$ interface with markings due to internal stacking faults on $\{110\}_\beta$ planes or $\{111\}$ f.c.c. Flewitt and Towner⁽⁸⁾ report this as a faulted f.c.c. structure while Warlimont⁽¹³⁾ claims it has the orthorhombic crystal structure of the martensite of the respective composition.

The microprobe work of Flewitt and Towner⁽⁹⁾ shows the rods precipitating with nearly the composition given by the equilibrium phase diagram. According to the recent kinetic analysis of Purdy⁽¹⁴⁾ it seems that their lengthening rates are diffusion controlled.

Hehemann and Repas⁽⁹⁾ have presented exhaustive growth data over the whole alloy compositional and temperature range including the needle-to-plate transition region; the plates forming at higher supersaturations

and lower temperatures. However, they could not justify the assumption of a diffusional growth mechanism using a Zener-Hillert lengthening model coupled with ideal thermodynamic solution behaviour. The plates grew several orders of magnitude too fast.

According to published microprobe work⁽⁸⁾ the plates have a decidedly non-equilibrium composition which initially is that of the matrix. As growth proceeds, and the plates thicken, the composition of the plate is reported to change and the adjacent matrix becomes progressively enriched in solute. This is also associated with the apparent annealing out of the stacking fault substructure. Warlimont⁽⁸⁾ suggests that there is little or no composition change when the plates first form and proposed that the growth rate is limited by the rate at which zinc could segregate to the closely-spaced faults. The driving force for the reaction is thought to be insufficient without the lowering of the stacking fault energy by the presence of the zinc. During annealing, the zinc could be rejected from the metastable plate. Garwood⁽¹³⁾ explains the approach to equilibrium via a surface rim through which zinc migrates from the interior of the plate. However, this requires diffusion up a thermodynamic gradient.

Flewitt and Towner⁽⁸⁾, following Christian⁽¹⁶⁾, would have the slower diffusing (immobile) species providing the framework for the shape change while the zinc accomplishes all the diffusion necessary for the transformation to take place. This is hard to imagine in a substitutional solid solution.

During prolonged annealing of the plates, the initially planar

interfaces bow outward into the matrix. This type of bulge could perhaps act as a nucleation site for secondary plates or even rods as the matrix becomes less supersaturated. Thus there is the possibility of plates exhibiting sideways degeneration into bundles of parallel rods. However, the growth rate of the original tip should still correspond to that of the true plate.

This account intends to show that a sheave of faceted needles grown at these temperatures in cross-section may well appear as a plate which is beginning to degenerate into needles. Experimentally this investigation is focussed on the relations between morphological change and composition change resulting in plate formation. Ultimately these observations will be used in support of a re-interpretation of published lengthening rates.

II THEORY

For the diffusion controlled migration rate of an interface under the condition of local chemical equilibrium, the velocity is determined in terms of the corrected diffusion coefficient (D_{eff}) and the concentration gradient normal to the interface (∇C_n) as:

$$v = - D_{eff} \nabla C_n / (C_{\beta} - C_{\alpha}) \quad (1)$$

C_{β} and C_{α} are the equilibrium interface concentrations.

Zener argued that a growing plate or needle would reject solute over a diffusion distance equal to its tip radius. Application of the above equation gives the tip velocity as:

$$v = \frac{D_{\beta}}{r} \cdot \frac{C_{\beta} - C_0}{C_{\beta} - C_{\alpha}} \left(1 - \frac{r_c}{r}\right) \quad (2)$$

Here the last term accounts for the effect of capillarity; a reduction of solute concentration at the tips of more sharply pointed precipitates. When $r = r_c$, the critical radius for nucleation, the diffusion gradient vanishes and $v = 0$. There is a multiplicity of solutions for this equation satisfying various values of r . Further refinements have not removed this indeterminacy but lead to a solution applicable to the isothermal growth of needles⁽¹⁰⁾:

$$\Omega_0 = \sqrt{\pi} \rho e^{\rho} \exp(-\rho) \left[1 + \frac{v}{v_c} \Omega_0 R_1(\rho) + \frac{r_c}{r} \Omega_0 R_2(\rho) \right] \quad (3)$$

or plates

$$\Omega_0 = \sqrt{\pi} \rho e^{\rho} \operatorname{erfc}(\sqrt{\rho}) \left[\left(1 + \frac{v}{v_c} \Omega_0 S_1(\rho) + \frac{r_c}{r} \Omega_0 S_2(\rho)\right) \right] \quad (4)$$

where

Ω_0 , the dimensionless supersaturation $\frac{X_{1\beta}^0 - X_{1\beta}^{\infty}}{X_{1\beta}^0 - X_{1\alpha}^0}$

ρ , the dimensionless velocity = $vr/2D$

v_c , the limiting velocity = $\mu_0 (C_{\beta} - C_{\alpha})$

where μ_0 , the kinetic coefficient depends on interface orientation.

$R_1(\rho)$, $R_2(\rho)$, $S_1(\rho)$, $S_2(\rho)$ are functions as tabulated by Trevedi.

The effect of non-ideality and interface curvature exerts the following condition for equilibrium across the interface⁽¹⁴⁾, α growing into β ,

$$X_{1\beta r} = X_{1\beta 0} \left[1 + \left(\frac{X_{2\beta 0}}{X_{1\alpha 0} - X_{1\beta 0}} \right) \left(\frac{2 \sigma V_\alpha}{r R T e_{1\beta}} \right) \right] \quad (5)$$

where:

V_α is the molar volume of α in β

σ is the interfacial energy

X_{ij}^k is the solubility of component i in phase j of curvature k

$e_{i\beta}$ is the thermodynamic factor = $1 + \frac{d \ln \gamma_{1\beta}}{d \ln X_{1\beta}} \Big|_{X_{1\beta}^0}$

Here the last term accounts for nonideality and curvature effects.

The appropriate diffusion coefficient is the unconstrained chemical diffusion coefficient approximated by $D_\beta^* e_{1\beta}$ where D^* is a tracer coefficient. The value of the critical radius is obtained by setting $X_{1\beta r} = X_{1\beta 0}$ in equation 5.

A plot of v vs. ρ and $\frac{r_c}{r}$ vs. ρ allows the choice of a unique solution if a constraint is chosen. It is customary to take that radius of curvature that maximizes the velocity. However, in the absence of a firm basis for this optimization other choices may be considered equally valid.

The affixing of numerical values to required parameters must be justified. The surface tension σ can be estimated as that of a high angle grain boundary for this system since the crystallography of the

plate tip indicates there is no lattice matching. This also allows the dropping of μ_0 term from equations 3 and 4 since there is negligible interface reaction compared to the driving force for diffusion. The other two terms involve the Ivanstov⁽¹⁸⁾ result for an iso concentrate dendrite and the correction for capillarity to this result.

The supersaturation is obtained from the equilibrium phase diagram for the system which however is questionable at lower temperatures. The molar volume, $\bar{V}_\alpha = X_{1\beta_0} \bar{V}_{1\alpha} + X_{2\beta_0} \bar{V}_{2\alpha}$, derives from the extrapolated molar volumes $\bar{V}_{1\alpha}$ and $\bar{V}_{2\alpha}$ and involves drawing a tangent to the curve of \bar{V} vs. X_{ij} . The thermodynamic factor e_{ij} is found from the slope of $\ln \gamma$ vs. X_{ij} at the concentration of interest. This changes drastically with the order-disorder temperature. Only limited experimental data are available for these empirical determinations of \bar{V}_α and e_{ij} .

III EXPERIMENTAL

A - Preparation of Materials

Alloys of various compositions were made by melting 99.999% copper and zinc bars (supplied by Cominco-Sheridan Park-Toronto) while under a sealed argon atmosphere. These were then water quenched and subsequently homogenized and requenched for the isothermal experiments. Small buttons were cut and if necessary, these were hammered to promote recrystallization during the precipitation experiments.

B - Procedure

The buttons were solutionized in the β region in air for an

appropriate time and then quenched into a salt bath at the required temperature for the isothermal precipitation reaction. These were then water quenched.

The alloys were then polished and subsequently deep-etched in alcoholic ferric chloride(anhydrous) for up to four hours.

In order to insure completely preferential etching, attempts were made to adjust the pH of the solution both chemically and electro-chemically.

Eventually it was found that a saturated solution worked best if there was a high volume fraction of precipitate (say 25%), especially in the case of the plates. Since needles are generally formed at the grain boundaries, etching them out was less difficult.

The precipitates were examined in a Cambridge Stereoscan II scanning electron microscope and analysed in situ by spot X-ray fluorescence, and subsequently analysed with a Cameca electron microprobe; both for copper and zinc in order to obtain the intensity ratio.

Growth kinetics were obtained by optically measuring the longest plate or rod observed on the entire sample. Attempts were also made to measure tip radii from stereoscan micrographs .

In the case of the 40.3 wt.% alloy, a single crystal was grown by directional freezing in order to polish close to the plane of growth of the plates⁽⁹⁾ and to encourage intergranular nucleation. This promoted the desired etching characteristics as there were no grain boundaries to be preferentially attacked.

IV RESULTS

Assuming that the maximum velocity criterion holds Hehemann and Repas' results can be reasonably well predicted with the previously described theoretical technique.

Again, only average values have been used for $e_{1\beta}$, D and σ . The results are plotted in Figure 2. It should be noted that theoretically the plate and needle kinetics differ but both fall within experimental scatter, although not on one line as Hehemann and Repas would indicate.

The maximum velocity criterion appears to be obeyed. Comparing the measured tip radii with those predicted (already done by Purdy for needles)⁽¹⁴⁾ was not possible because of the poor resolution of the scanner but the technique has been proven. However, there is agreement with the single measurement recorded by Hehemann and Repas who reported a tip radius of 425 - 475 \AA for the 42.5% Zn alloy at 250° C. The calculated value, derived from the critical radius ratio at the maximum velocity is available from the plotted outputs (Figure 14, 15), where the critical radius = 71.3 \AA for needles and 35.7 \AA for plates.

Assuming the actual morphology lies between that of a needle or plates, this gives a range of expected tip curvature of 370 \AA - 550 \AA respectively.

In general optical metallography is more preferable to scanning electron microscopy for the determination of growth. This is because good contrast does not occur until high magnification (2000 X) and a critical inclination to the electron beam is achieved.

It has also been found that groups of closely spaced or inter-connected needles also form in this system as shown in the micrographs. In cross section, these appear to be the plates which co-exist at 250° C. It is possible that what Flewitt and Towner⁽⁸⁾ refer to as evidence for plate breakdown into needles is actually a section of a sheave of needles. The scanning electron micrographs indicate the true shape of the features seen in planar metallographic sections. (The photographs show the deep etched morphology of the plates) the few grain boundary needles at this temperature are very long, narrow and faceted. Note the remaining scratches; these are evidence of minimal attack of the α phase by the etchant.

Electron probe microanalysis of the deep etched (and unattacked) plate tips reveals partitioning up to 6 wt.% which again supports a diffusional mechanism.

The large matrix needles at this temperature also show the same partitioning at the tip.

The etching was checked by going through focus at the plate tip with a maximum count at the mid-focus position. Hence the matrix was not interfering with the analysis. Since the matrix was only about 25% transformed the actual partitioning is observable.

By positioning the plate perpendicular to opposed spectrometers, simultaneous counting for both copper and zinc is possible, allowing the calculation of an intensity ratio. There is no matrix interference.

because of the deep etch and the take-off angle of the probe. Hence no corrections for this need be made. The beam current was stable throughout the counting periods and the counts were standardized after each measurement. The probe output shows the repeatability. Quantitative analysis for copper and zinc separately does not total up to 100%. This is probably due to the small volume analysed; the intensity ratios for Cu and Zn should give accurate chemical analysis. The X-ray spot fluorescence analysis was attractive being in situ. This allowed a micrograph to be taken of the exact position being sampled. However, the analysis is taken by electronically sampling every 2 ev. which thus gives a band width rather than discrete focus. The result is a somewhat erratic counting for Cu and Zn near their respective $K\alpha_1$ voltages (Table II A). However, the trend to partitioning was definitely there but did not allow a quantitative approach.

One of the most convincing arguments for zinc partition during plate growth stems from the similar chemical analyses obtained for needles and plates. If the etching technique changed the α composition appreciably, analysis of the needles would not yield the correct equilibrium compositions. It is probable that Flewitt and Towner analyzed plates so small that matrix effects initially obscured the composition change attending plate growth.

PART II

Bainitic Steels

I Introduction

The lengthening kinetics of upper bainite in iron-carbon alloys conform approximately to a Zener-Hillert analysis⁽²⁾. A major source of uncertainty lies in the extrapolated phase equilibria but it appears that the metastable binary phase boundaries govern the transformation. Thus a local equilibrium model appears to be appropriate. Hehemann has argued that the observable effects of alloying elements cannot be explained with a volume diffusion model. There are various ideas concerning the nature of the bainite reaction. These include; a slow growing martensite; carbide precipitation control; repeated nucleation of a subunit; and partitioning of carbon ahead of the interface under diffusion control.

For diffusion-controlled growth from alloyed austenite, two alternative methods have been proposed for the determination of the interfacial carbon content. Both insist that the alloying element does not partition during precipitate growth from highly supersaturated austenite and that the carbon activity is continuous across the austenite ferrite interface. Hultgren⁽¹⁹⁾ and Hillert⁽²⁰⁾ introduced the concept of para-equilibrium in which the alloying element is essentially an inert diluent. This concept is similar to Aaronson's no partition equilibrium calculations⁽²¹⁾. The thermodynamic boundary condition involves a

free energy minimum subject to the constraint that the para-equilibrium tie-line must coincide with a component ray (Fig. 7). Hence the transformation can take place under pure carbon diffusion control and yet not be in true local equilibrium; the tie-lines being parallel to the carbon axis (Fig. 6).

Hehemann⁽²⁾ questions the application of this model when comparing measured growth kinetics to those calculated by Rao and Winchell⁽²²⁾ for the para-equilibrium boundary condition; in particular, the addition of 10% nickel to austenite gives true upper bainite at 400 °C but the measured growth rate is too slow. Local equilibrium solutions exist but predict vanishingly small rates because their system points were taken above the solubility limit of nickel in ferrite, in a regime where nickel should partition.

The other approach involves an extension of the local equilibrium model to ternary systems in which the two solutes diffuse at much different rates (substitutional and interstitial). This requires the presence of an alloying element 'spike' at the phase boundary which controls the carbon activity of the interface. The result is an envelope of no-partition within which the carbon activity will be higher at the interface than in the interior of the γ grain during initial stages of transformation.⁽²³⁾ This activity gradient supplies the driving force for carbon diffusion (Fig. 8, 9).

Assuming that this alloy spike has some penetration into the parent phase, Hillert⁽²⁴⁾ suggested that with increased interface velocity (i.e. higher supersaturation) the spike must retreat into the interface (Fig. 10). However, as long as the product phase is in equilibrium with the enriched boundary, the local equilibrium model remains a valid description with the effective interfacial carbon concentration being adjusted by the thermodynamic interaction with the "spike". This interaction is measured by the Wagner parameter, ϵ_{12} .

Hence the alloying element effect becomes an impurity drag effect, but one which is calculable on this hypothesis from knowledge of the ternary phase field.

IIb Theory

The para-equilibrium phase boundaries for the iron-rich region of the Fe-C-Ni phase field at 400° C have been theoretically determined from thermodynamic calculations for a range of temperatures and composition including extrapolation to low temperatures⁽²²⁾.

Since the binary limits of the Fe-Ni and Fe-C systems are available at these temperatures the slope of the limiting phase boundaries of the ternary isotherm can be calculated at the solubility limits after the method of Purdy (see Appendix I) from the known binary partition coefficients K_i and the interaction parameters ϵ_{ij}

i.e.:

$$\frac{\partial C_2}{\partial C_1} \Big|_{C_1^{\alpha} \rightarrow 0} = - \left[\frac{1 - \frac{1}{K_1}}{1 - \frac{1}{K_2}} + \epsilon_{12}^{\alpha} C_2^{\alpha} \right] / \left[1 + \epsilon_{22}^{\alpha} C_2^{\alpha} \right]$$

and

$$\frac{\partial C_1}{\partial C_2} \Big|_{C_2^{\alpha} \rightarrow 0} = - \left[\frac{1 - \frac{1}{K_2}}{1 - \frac{1}{K_1}} + C_1^{\alpha} \epsilon_{12}^{\alpha} \right] / \left[1 + \epsilon_{11}^{\alpha} C_1^{\alpha} \right]$$

Because the phase field is wide the partition coefficients are the governing terms and hence the phase boundary is linear (in the case of dilute α). From this the chemical potential difference of carbon associated with the para-

equilibrium and local equilibrium phase boundaries for the α can be used to predict the shift of the para-equilibrium phase boundary relative to the no partition line and is given by: (see diagram, Fig. 12)

Local equilibrium at the interface requires equality of chemical potentials across it

$$M_{1\alpha}^{\rho} = M_{1\beta}^{\rho} \quad \rho - \text{para-equilibrium}$$

$$M_{1\alpha}^N = M_{1\beta}^N \quad N - \text{no partition}$$

Then

$$M_{1\alpha}^{\rho} - M_{1\alpha}^N = M_{1\beta}^{\rho} - M_{1\beta}^N$$

In general the partial molar free energy can be written as:

$$M_{1\alpha}^{\rho} = M_{1\alpha}^{\circ} + RT \ln \gamma_{1\alpha}^{\rho} C_{1\alpha}^{\rho}$$

Applying the Wagner expansion gives

$$\ln \gamma_2 = \ln \gamma_2^{\circ} + \epsilon_{21} C_1 + \epsilon_{22} C_2$$

Then

$$\ln C_{1\alpha}^{\rho} + \ln \gamma_{1\alpha}^{\rho} = \ln \gamma_{1\alpha}^{\circ} + \epsilon_{11\alpha} C_{1\alpha}^{\rho} + \epsilon_{12\alpha} C_{2\alpha}^{\rho} + \ln C_{1\alpha}^{\rho}$$

Similarly

$$M_{1\alpha}^N = M_{1\alpha}^{\circ} + RT \ln \gamma_{1\alpha}^N C_{1\alpha}^N$$

and

$$\ln \gamma_{1\alpha}^N + \ln C_{1\alpha}^N = \ln \gamma_{1\alpha}^{\circ} + \epsilon_{11\alpha} C_{1\alpha}^N + \epsilon_{12\alpha} C_{2\alpha}^N + \ln C_{1\alpha}^N$$

then

$$\epsilon_{12\alpha} (C_{2\alpha}^{\rho} - C_{2\alpha}^N) + \epsilon_{11\alpha} (C_{1\alpha}^{\rho} - C_{1\alpha}^N) + \ln C_{1\alpha}^{\rho} / C_{1\alpha}^N =$$

$$\epsilon_{11\beta} (C_{1\beta}^{\rho} - C_{1\beta}^N) + \ln C_{1\beta}^N / C_{1\beta}^{\rho} + \epsilon_{12\beta} (C_{2\beta}^{\rho} - C_{2\beta}^N)$$

↗ 0
↗ small
↗ 0

$$\text{Therefore } \ln \frac{C_{1\alpha}^P}{C_{1\alpha}^N} = \epsilon_{11\beta} (C_{1\beta}^P - C_{1\beta}^N) + \ln \frac{C_{1\beta}^P}{C_{1\beta}^N}$$

Thus $C_{1\beta}^N$ can be solved.

here: ϵ_{ij} = the Wagner interaction coefficients

M_j = the chemical potentials

γ_{ij} - the activity coefficients

C_{ij} - the concentrations

This then alleviates the need to calculate the carbon-rich true equilibrium phase boundary for the γ phase and then follow an isoactivity line for carbon as is generally prescribed. This actually involves the extension of the carbon isoactivity line for the austenite phase into the two phase region until it intersects the immobile solute isocomposition line. This point then gives the effective carbon concentration for the transformation. In the limiting case, and under ideal conditions, the isoactivity line would be parallel to the nickel axis.

From this theoretical phase diagram the carbon supersaturation can be obtained and hence the growth rate can be calculated by the same means as previously described (since the carbon supersaturation supplies the driving force).

II.a Calculations of the Fe-C-X Isotherm.

The best extrapolated values for the slope of the α binary limits are obtained from Aaronson et al⁽⁴⁾ which also gives the required partition

coefficients. The para-equilibrium phase boundaries have been calculated by Rao et al⁽²²⁾. However, from the literature there is some range for the choice of the extrapolated Fe-C austenitic phase field at 400° C⁽²⁸⁾. Hence the para-values are used (as the two solutions coincide at the boundary limit) Thus the no-partition line can be calculated from the previously described mathematical technique without the use of the "rich" γ phase boundary. An expanded scale was used in the α region to find the concentration parameters required in the calculations.

II.b Kinetic Calculations

Again Trevedi's solution was applied to the system assuming that the driving force is supplied by effective carbon supersaturation. Calculations are made on the computer (C.D.C. 6400) both with local equilibrium no partition and para-equilibrium applying at the tip using the tie-lines of the theoretically constructed phase diagram. The weighted average diffusion coefficient of carbon in the matrix was calculated following the method of Trevedi and Pound⁽²⁵⁾, and is of the form

$$\int_{C_0}^{C_i} \frac{D}{C_i - C_0} dC$$

Here the diffusivity, D , is a function of concentration as given by Cohen et al⁽²⁶⁾ involving the multiplication of concentration dependent exponential functions.

A technique was also worked out to find the interaction parameter $e_{1\beta}$:

$$e_{1\beta} = 1 + \frac{\partial \ln \gamma_{1\beta}}{\partial \ln C_{1\beta}}$$

the Wagner expansion of $\ln \gamma_1$ gives

$$\ln \gamma_1 = \ln \gamma_1^0 + \epsilon_{11} C_1 + \epsilon_{12} C_2$$

constant | constant for no partition

differentiating

$$\frac{\partial \ln \gamma_1}{\partial \ln C_1} = \frac{\epsilon_{11} \partial C_1}{\partial \ln C_1} = \epsilon_{11} C_1$$

then

$$e_{1\beta} = 1 + C_{1\beta}^{\infty} \epsilon_{11}$$

|
Bulk concentration

III Experimental

The alloys were prepared from electrolytic iron and nickel (99.9%) melted and remelted in a non-consumable tungsten electrode arc furnace under an argon atmosphere. These were then homogenized as specified by calculation using the method of Purdy and Kirkaldy⁽²⁷⁾, and then quenched to martensite or martensite plus austenite. Thin sections were re-austenitized in air and quenched into a salt bath at 400° C for the required growth (nucleation time must also be accounted for) and then water quenched. The heat treatment time and temperature were carefully chosen to allow 100% re-austenitizing, maximum

grain growth after recrystallizing and minimum oxidation and decarburizing. The specimens were dropped directly into a salt bath beneath the furnace. Knoop hardness tests ensured that martensite or retained austenite was obtained on the final water quench. Specimens were polished and etched in picral to reveal the bainite rods. The growth kinetics were measured using the longest visible rod technique with optical metallography.

IV Results

The calculated ternary isotherm is shown in Fig. 11. Using the carbon supersaturation from the no partition local equilibrium model, satisfactory kinetics can be generated for intermediate supersaturations. As the 'phase' boundary is approached the velocity should approach zero if local equilibrium is maintained by the system. Since it does not, this implies that the impurity drag model which departs from the local equilibrium mode, at this point is appropriate.

In all cases the growth rate was too slow for para-equilibrium to apply. However, the difference was a constant factor throughout the range of supersaturation. All of the present results were within a factor of the para-equilibrium calculation. However, at higher nickel contents, para-equilibrium fails conclusively.

DISCUSSION

The ideal solution model for the diffusion-controlled growth of plates or needles is inadequate to describe non-ideal (i.e. non-dilute) binary behaviour. A thermodynamic factor must be included in the effective diffusivity and critical radius. The thermodynamic factor $(1 + \frac{\partial \ln \gamma}{\partial \ln C})$ enters the growth rate as a squared term, and since this factor can become large (~20) in systems tending to order, it can effect calculated growth rates by 2 or 3 orders of magnitude. Trevedil's solution of the diffusion equation for a non-isoconcentrate paraboloid of revolution incorporates a capillarity term which can accommodate non-ideal thermodynamic behaviour.

If the growth of the precipitating phase in a ternary dilute solution is governed by the diffusional behaviour of the interstitial component, the kinetics can be treated as binary. Thermodynamic interaction can also be included into this model.

Kinsmen, Aaronson and Laird, in their excellent review⁽²⁹⁾ generally discounted a martensitic motion in the formation of α plates from β brass, but were unable to account for the high rates. The microprobe and kinetics results of this investigation support their viewpoint, and show how a simple diffusional growth model can rationalize previously unexplained behaviour. The chemical analysis of the isolated plate tip shows immediate partitioning of the zinc.

The massive transformation in this system occurs as a well-aligned faceted sheave of needles which in cross-section resembles the plate cross-

section and has the same analysis. However, the faceting is much coarser than that of the plates. Other workers⁽³⁰⁾ may have presented micrographs of this faceting as indicating morphological breakdown and have then intimated that the plates grow in accordance with calculated needle kinetics. Hence Hehemann and Repas' observations can be supported by noting that the plate has a very fine substructure and a definite diffusional lengthening kinetics of its own. Once breakdown occurs, the sideways growth rate is probably needle-like in character. A surface grown plate or needle does not reveal the true nature of an internally constrained species (i.e. one grown in bulk material)

With higher resolution, the deep-etching technique should reveal the tip curvature as well as any faceting which the plates may assume. This could then lead to a crystallographic explanation for the nature of the needle-to-plate transition. The plates, being intragranular, possibly have a more rigidly controlled orientation relationship and morphology.

It appears that the alloy bainite growth kinetics are diffusionaly controlled under the assumption of a modified local equilibrium criterion. At most supersaturations the no-partition local equilibrium model is well-obeyed but not at the "phase" boundary (i.e. the envelope of zero partition).

The concept of solute drag bears consideration here in that it may be involved in the true equilibrium and become effective at higher carbon content i.e. lower supersaturation. In this system there is a positive interaction between the solutes which thermodynamically increases the effective carbon concentration and hence the driving force and velocity.

The free energy required for a transformation is used to overcome curvature effects, interfacial friction and diffusion and is supplied by the

chemical potential change (supersaturation) for the reaction. If the diffusivity and interactivity of the substitutional element in the Fe-C-X system affects the driving force for the reaction, the existence of a boundary "phase" (viz: grain boundary) can be used to explain the observed velocity of the reaction. The alloying element need not partition in this case but rather piles up ahead of the interface inside the boundary region. This situation then also controls the carbon activity at the interface. At this point this model and the local equilibrium no-partition model are the same.

If the kinetic factors connected with the transport of carbon are rapid enough in comparison with the rate of diffusion of the alloying element, the growth rate may be so high that the thickness of the pile up may only exist mathematically (even though the boundary region still exists physically). Here a deviation from local equilibrium begins to develop as the free energy loss decreases and goes to zero. The effect of the alloying element will now be quite small. Thus the realm of para-equilibrium would be entered.

As the carbon supersaturation decreases along an isoconcentration line of the alloying element the growth rate will slow down. Hence the concentration profile of the alloy spike will widen inside the boundary area and eventually become step like. Local equilibrium can be maintained on the α side of the boundary because the diffusivity of nickel in the boundary is much faster than in austenite. It follows that the penetration of the nickel profile into the surrounding matrix will be quite small. There may also be a gradient within the boundary phase depending on the velocity. The carbon concentration profile will be controlled by that of the alloying element through chemical

interaction. Hence local equilibrium can be maintained at the α interface while carbon is rejected into the surrounding austenite down the boundary gradient. This constitutes a deviation from the local equilibrium no-partition model. As the phase boundary (envelope of zero partition) is approached, the boundary phase becomes rate controlling and may force the carbon to maintain a concentration spike through it even though the theoretical supersaturation has gone to zero under the forementioned condition. Hence the growth could still continue at an appreciable rate without partitioning of the nickel. Higher carbon content experiments should reveal a continuous decrease in the velocity and eventual entrance into true equilibrium in which the ternary tie-lines are obeyed both for nickel and carbon. At this time the velocity will virtually go to zero at the temperature of interest.

The postulation of maximum velocity is not the only possible one. Other criteria include maximum transformed volume and maximum or minimum entropy production rate. However, within the experimental technique, the assumption does seem to lead to a predictable result.

SUMMARY

The growth rates of the precipitation of alpha needles and plates from supersaturated beta brass have been examined. A refined Zener-Hillert diffusion controlled model was used to analyse this and included corrections for the non-dilute system. The application of a maximum velocity condition allowed the prediction of the rate of transformation over the whole range of temperature and composition. The morphology and chemistry of the plates was clarified and indicated that the growing tip was a true diffusional product.

The kinetics of $\gamma \rightarrow \alpha$ upper bainite growing in the Fe-C-Ni system were analysed. This required the construction of the applicable ternary phase field dependent on the choice of a suitable model. Both the paraequilibrium and local equilibrium no partition approaches were taken using a similar technique as that found suitable for the brasses. The compositions chosen resulted in a growth rate which was too fast for the diffusion of nickel to occur under chemical equilibrium constraints. Although the local equilibrium no-partition model applies over intermediate supersaturations, it is hypothesized that a solute drag model is required outside the envelope of zero partition (both concepts are interchangeable inside this envelope).

The results however, were considered consistent with the possible effects of alloying elements on a diffusionaly regulated bainitic transformation in low carbon steels.

CONCLUSIONS

- (1) The growth of α plates and rods in β -brass is well described by a local equilibrium model with corrections for non-ideal thermodynamic behaviour. This is also supported by microprobe analysis of the extracted plate tip which shows immediate partitioning of the zinc.
- (2) The deep etching technique should also reveal crystallographic information on the needle-to-plate transition as well as permit the measurement of tip radii.
- (3) Alloy bainite lengthening rates are also consistent with the local equilibrium model but the concept of impurity drag is required to understand measured rates for high nickel content alloys. However, the measuring technique must be refined and more experiments should be done if the paraequilibrium boundary condition is to be firmly discredited for this composition range and temperature.

APPENDIX

From Purdy⁽³⁸⁾ the expression for the slope of the α phase boundary at the binary limits is of the form:

$$\frac{dC_1}{dC_2} \cdot \left[\frac{1}{C_1^\alpha} + \epsilon_{11}^\alpha + \epsilon_{12}^\alpha \frac{C_2^\alpha}{C_1^\alpha} \left(\frac{1 - \frac{1}{K_2}}{1 - \frac{1}{K_1}} \right) \right] =$$

$$- \left[\epsilon_{12}^\alpha + \epsilon_{22}^\alpha \frac{C_2^\alpha}{C_1^\alpha} \frac{1 - \frac{1}{K_2}}{1 - \frac{1}{K_1}} + \frac{1}{C_1^\alpha} \left(\frac{1 - \frac{1}{K_2}}{1 - \frac{1}{K_1}} \right) \right]$$

multiply through by C_1^α and let $C_1^\alpha \rightarrow 0$

$$\text{then } \frac{\partial C_1}{\partial C_2} \cdot \left[1 + \epsilon_{12}^\alpha C_2^\alpha \frac{1 - \frac{1}{K_2}}{1 - \frac{1}{K_1}} \right] = - \left[\epsilon_{22}^\alpha C_2^\alpha \frac{1 - \frac{1}{K_2}}{1 - \frac{1}{K_1}} + \frac{1 - \frac{1}{K_2}}{1 - \frac{1}{K_1}} \right]$$

divide through by $1 - \frac{1}{K_2} / 1 - \frac{1}{K_1}$

$$\text{then } \frac{\partial C_1}{\partial C_2} \left[\frac{1 - \frac{1}{K_1}}{1 - \frac{1}{K_2}} + \epsilon_{12}^\alpha C_2^\alpha \right] = - \epsilon_{22}^\alpha C_2^\alpha + 1$$

$$\text{or } \frac{\partial C_2}{\partial C_1} \stackrel{C_1^\alpha \rightarrow 0}{=} - \left[\frac{1 - \frac{1}{K_1}}{1 - \frac{1}{K_2}} + \epsilon_{12}^\alpha C_2^\alpha \right] / \left[1 + \epsilon_{22}^\alpha C_2^\alpha \right]$$

for $C_2^\alpha \rightarrow 0$ a similar manipulation gives

$$\frac{\partial C_2}{\partial C_1} \stackrel{C_2^\alpha \rightarrow 0}{=} - \left[1 + \epsilon_{11}^\alpha C_1^\alpha \right] / \left[C_1^\alpha \epsilon_{12}^\alpha + \frac{1 - \frac{1}{K_2}}{1 - \frac{1}{K_1}} \right]$$

For the case of Fe-C-Ni,

$$\frac{\partial C_2}{\partial C_1} \Big|_{C_{2\alpha} \rightarrow 0} \approx \frac{\partial C_2}{\partial C_1} \Big|_{C_{1\alpha} \rightarrow 0}$$

As the distribution coefficients are the major factors (K_1, K_2).

Hence the α phase boundary is approximately linear.

REFERENCES

- (1) E. S. Davenport and E. C. Bain: Trans. AIME 90, 117, 1930.
- (2) R. F. Hehemann: Ch. 9 of Phase Transformations ASM 1970.
- (3) H. I. Aaronson: the Mechanism of Phase Transformation in Crystalline Solids, Institute of Metals, London 1969, pg. 289.
- (4) H. I. Aaronson, H. A. Domian, G. M. Pound: Trans. AIME 236, 753, 1966.
- (5) K. R. Kinsman, H. I. Aaronson, E. Eichen: Met. Trans. 2, 346, 1971.
- (6) P. E. J. Flewitt & J. M. Towner: Acta Met. 15, 943, 1967.
- (7) R. D. Garwood: J. Inst. Metals 83, 64 1954.
- (8) P. E. J. Flewitt & J. M. Towner: J. Inst. Metals 95, 273, 1967.
- (9) P. E. Repas & R. F. Hehemann: Tech. Report # 6 to U.S. Office of Naval Research, Contract Nonr. 1141 (5) 1967.
- (10) R. Trevedi: Metall. Trans 1, 921, 1970.
- (11) H. M. Clark & C. M. Wayman: Ch. 2 of Phase Transformations ASM 1970.
- (12) P. E. J. Flewitt: Scripta Meta. 2, 161, 1968.
- (13) R. D. Garwood: Physical Properties of Martensite and Bainite Special Report 93 ISI, London 1965, pg. 92.
- (14) G. R. Purdy: Metal Science Journal 5, 81, 1971.
- (15) E. Hornbogen and H. Warlimont: Acta Met. 15, 943, 1967.
- (16) J. W. Christian: Decomposition of Austenite by Diffusional Processes, Interscience, New York, 1962, pg. 371.
- (17) C. Zener: Trans. AIME 167, 550, 1946.
- (18) G. P. Ivantsov: Doklady Akad Nauk SSR 132, 1307, 1960.

- (19) P. Hultgren: Jernkontorets Annaler 135, 403, 1951.
- (20) M. Hillert: Jernkontorets Annaler 136, 25, 1952.
- (21) H. A. Aaronson, H. I. Domian, G. M. Pound: Trans AIME. 236
768, 1966.
- (22) M. M. Pao, R. J. Russell, P. G. Winchell: Trans AIME 239,
634, 1967.
- (23) G. R. Purdy, D. H. Weichert & J. S. Kirkaldy: Trans AIME 230,
1025, 1964.
- (24) M. Hillert: The Mechanism of Phase Transformations in Crystalline
Solids - Symposium Inst. of Metals, 1969, pg. 231.
- (25) R. Trevedi, G. M. Pound: J. A. P. 38, 3569, 1967.
- (26) L. Kaufman, S. W. Radcliffe, M. Cohen: Decomposition of Austenite
by Diffusional Processes, Interscience, New York, 1962, pg. 313.
- (27) G. R. Purdy & J. S. Kirkaldy: Metall. Trans 2, 371 1971.
- (28) H. I. Aaronson & H. A. Domian: Trans AIEE 236, 781, 1966.
- (29) H. I. Aaronson, C. Laird, K. R. Kinsman: Ch. 8 of Phase Transformations
ASM 1970.
- (30) P. E. J. Flewitt: The Mechanism of Phase Transformation in Crystalline
Solids, Inst. of Metals, London 1969, pg. 90.
- (31) Smith R. P. 1946, J. Am. Chem. Soc., 68, 1163.
- (32) Smith R. P. 1948, J. Am. Chem. Soc., 73, 2724.
- (33) R. Hultgren, R. L. Orr, P. D. Anderson, K. K. Kelley,
"Selected Values of Thermodynamic Properties of Metals and
Alloys", Wiley (1963).
- (34) W. B. Pearson, "Handbook of Lattice Spacings and Structures of
Metals and Alloys", Vol. 2, Pergamon (1967).
- (35) A. B. Kuper, D. Lazarus, J. R. Manning and C. T. Tomizuka,
Phys. Rev., 104, 1536.

- (36) T. B. Massalski and J. E. Kittl., J. Aust. Inst. Metals, 1963, 8, 91.
- (37) M. Hansen, "Constitution of Binary Alloys", 2nd. Ed., McGraw-Hill (1958)
- (38) G. R. Purdy: Private Communication 1970.

TABLE I (a)

ACTIVITY DATA FOR Fe-C-NI SYSTEM

<u>Parameter</u>	<u>Value</u>	<u>Source</u>
ϵ_{11}^{α}	5.0	Smith 1946
ϵ_{22}^{α}	5.0	assumed ideal
ϵ_{12}^{α}	4.9	Smith 1948
ϵ_{11}^{β}	8.9	Smith 1946
$1/K_1$	200	Rao et al
$1/K_2$	6	
$C_{1\alpha}$	7.2×10^{-4}	
$C_{2\alpha}$.056	
$\sigma_{\alpha\beta}$	750 ergs/cm ²	Estimated (disordered)
V_{α}	7 cm ³ /mol.	Molar Vol. of Iron
\bar{D}_c^Y		K. R. C.

I (b)

ACTIVITY DATA FOR Cu-Zn SYSTEM

$\epsilon_{1\beta}$	13	Hultgren et. al
σ	500 ergs/cm ²	Estimated from σ G.B.
V_{α}	7.75 cm ³ /mol.	Pearson
D_{β}^*		Kuper et. al.

TABLE II

SUMMARY OF MICROPROBE ANALYSIS

Cu 40.3 wt.% Zn (250° C)

		Cu	Zn	
I	REFERENCE	Counts	Counts	
		2J791	7116	
		23627	7087	
		<u>2J598</u>	<u>7122</u>	
		23669	7108	AVERAGE
II	NEEDLE	15877	1789	
		14721	1784	
		<u>14746</u>	<u>1833</u>	
		15115	1802	AVERAGE
III	MATRIX	13770	2640	
		13195	2647	
		13784	1462	
		13920	2467	
		13907	2449	
		139J2	2J43	
		13571	2543	
		12809	2526	
		12880	2558	
		<u>13939</u>	<u>2583</u>	
		13580	2522	AVERAGE

IV	PLATE	15353	2243	
		15062	2243	
		15127	2092	
		15509	2189	
		15622	2079	
		15846	2005	
		14149	2084	
		14073	1965	
		14844	1971	
		<u>14842</u>	<u>2006</u>	
		15040	2086	AVERAGE

BASED On % Cu or % Zn x $\frac{23669}{7108}$

INTENSITY RATIOS ANALYSIS:

		Cu	Zn
2.4:1	NEEDLE	71	29
1.62:1	MATRIX	62	38
2.16:1	PLATE	68	32

TABLE II - A

IN SITU X-RAY FLUORESCENCE SPOT ANALYSIS
FROM SCANNING ELECTRON MICROSCOPE.

	Counts Cu	Counts Zn
<u>MATRIX</u>	945	356
	928	366
	926	251
<u>PLATE</u>	765	350
	909	471
	847	452

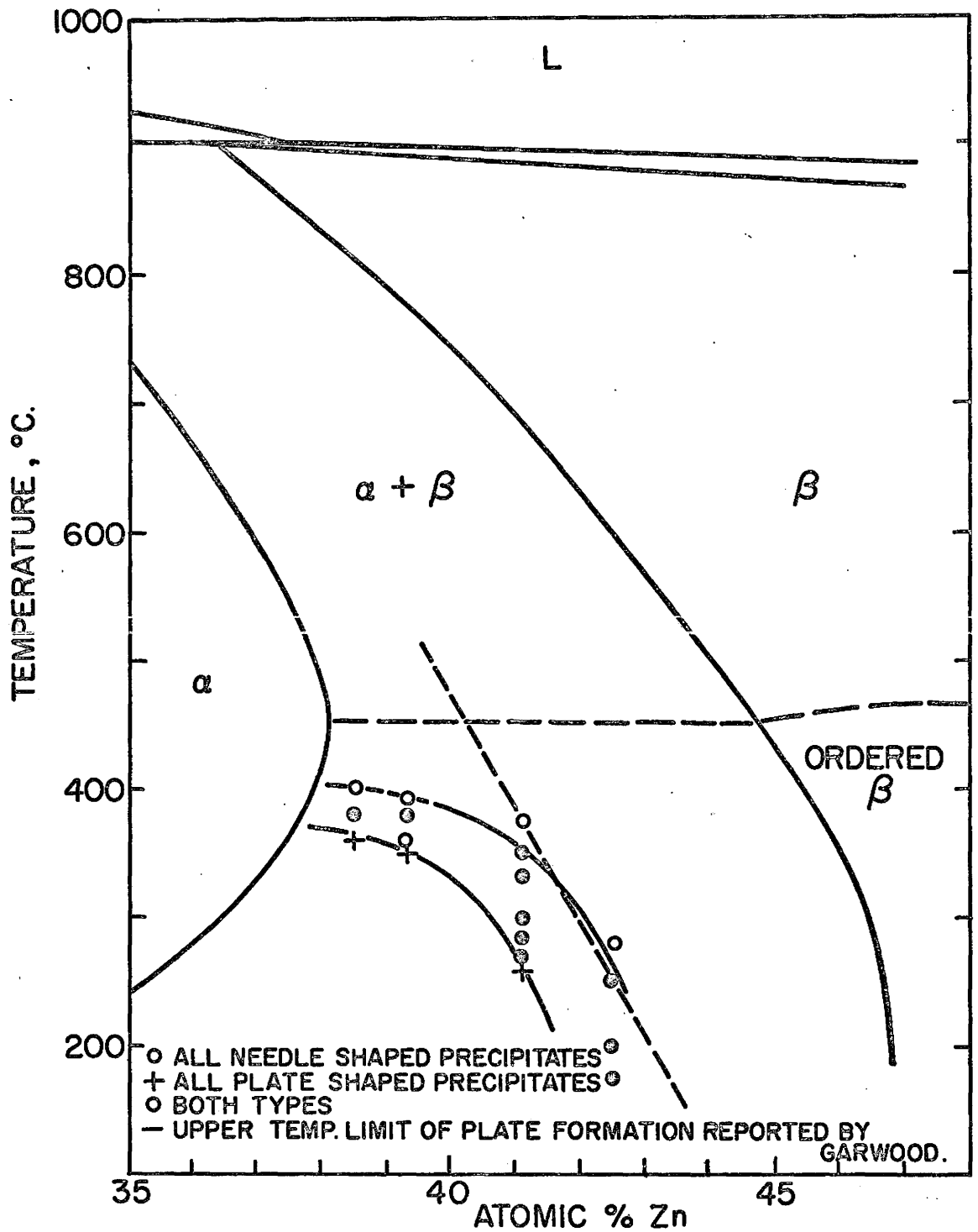


Figure 1. THE COPPER-ZINC EQUILIBRIUM DIAGRAM FROM 35 TO 48 % ZINC - AFTER MASSALSKI, KITTL AND HANSEN.

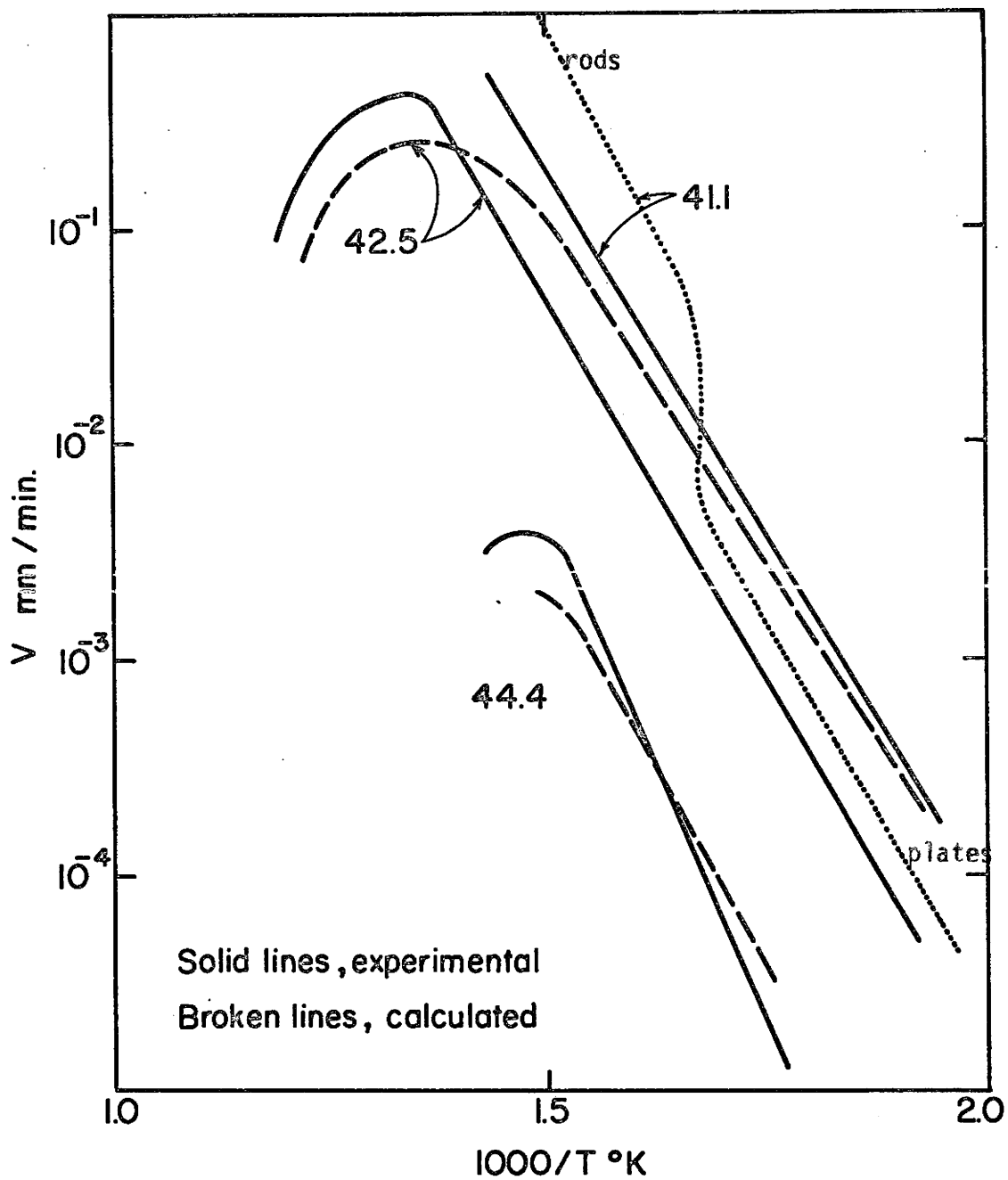
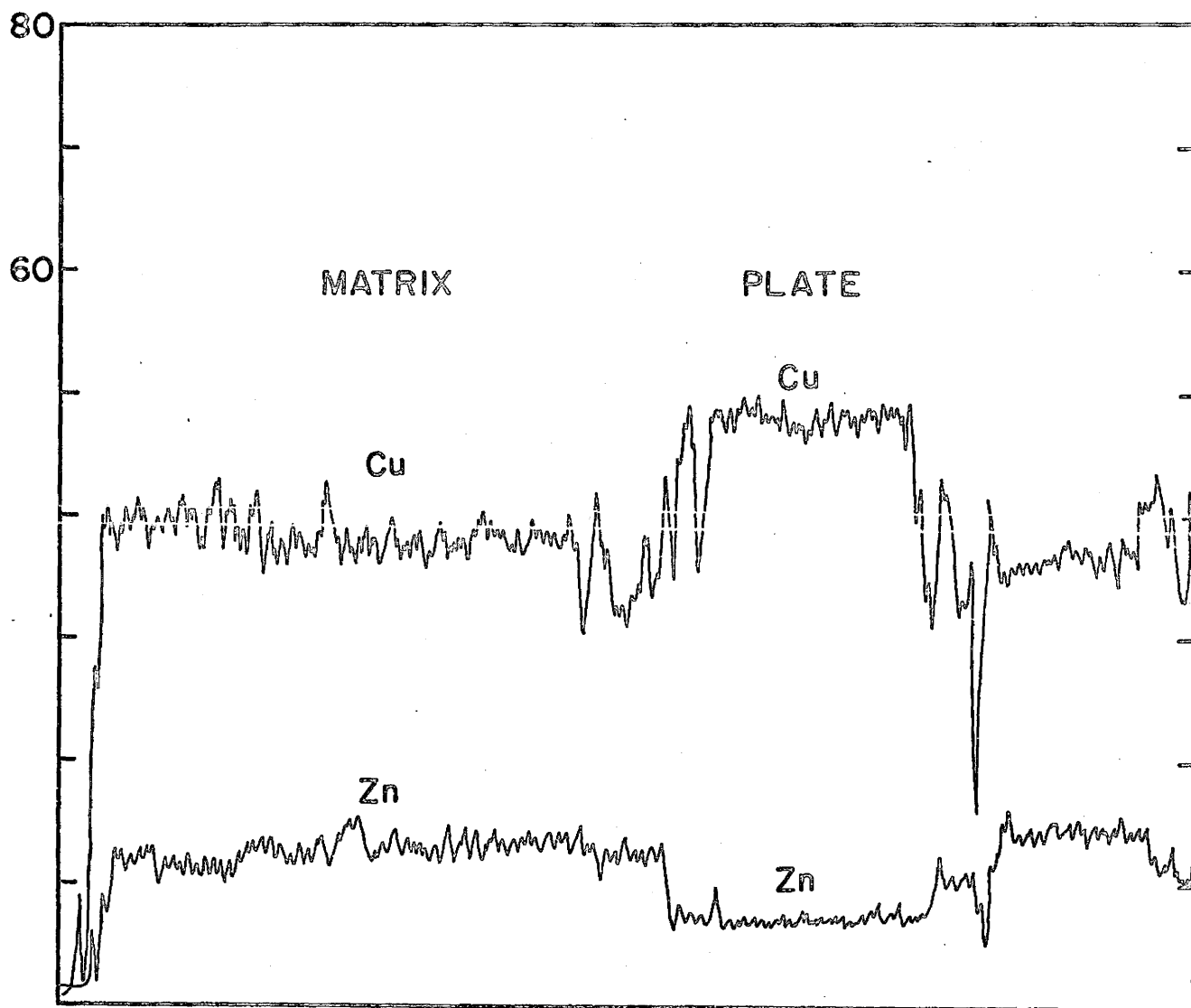


Figure II. Comparison of calculated and published experimental growth rates of α plates and rods in β -brass showing rod to plate transition for the 41.1 case.



MICROPROBE ANALYSIS OF ISOLATED α PLATE, 250°C.

Figure III.

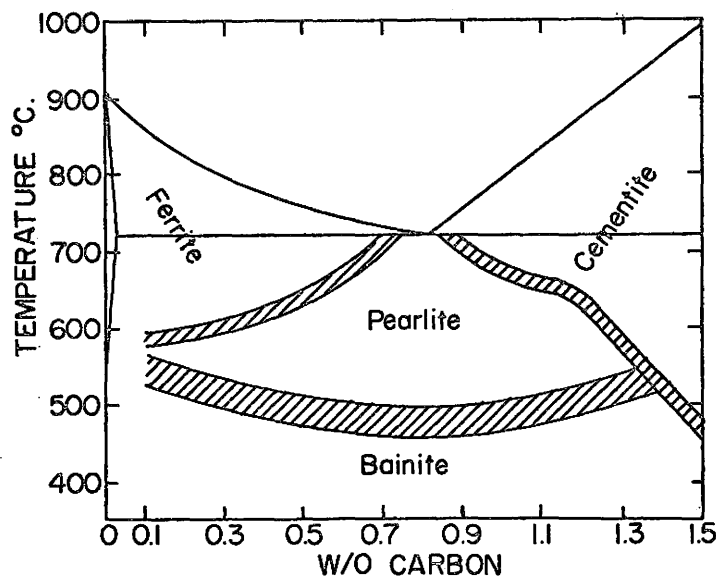
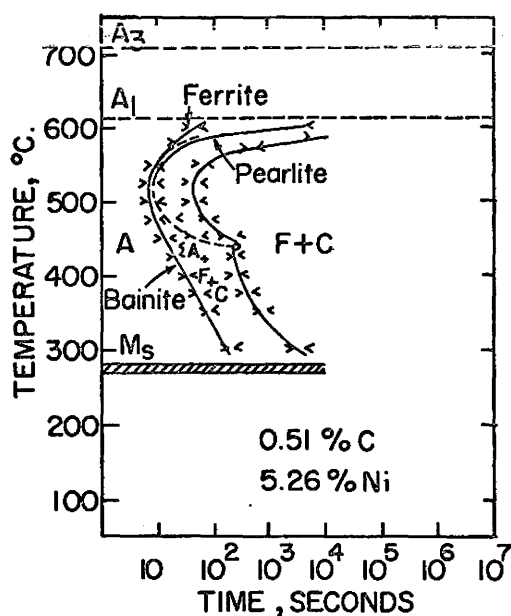
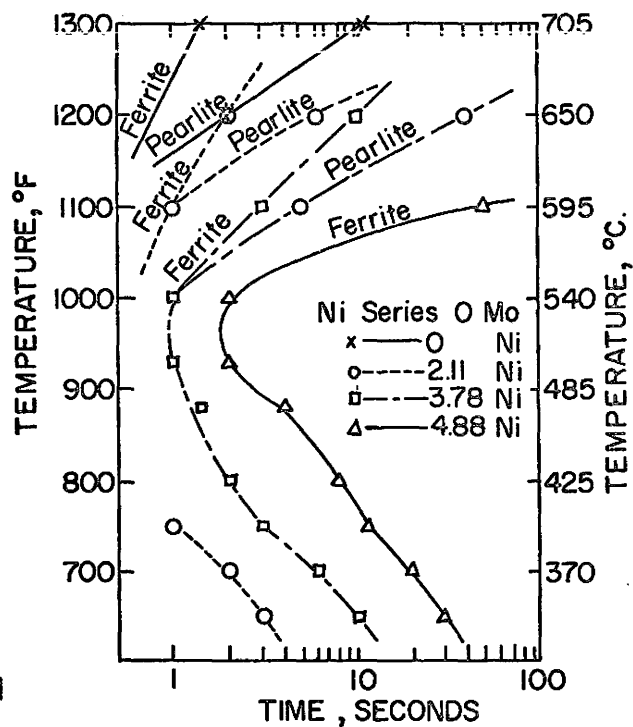


Figure IV. Temperature-composition regions in which the ferrite, cementite, pearlite, and bainite reactions are dominant in plain-carbon steels.



0.51% carbon- 5.26% nickel steel



0.55% carbon pure iron-nickel alloy
C-0.55 - Ni-3.78

Figure V. T.T.T. curves for Fe-C-Ni system at composition-range of interest (from Atlas of Isothermal Transformation Diagrams Supplement, U.S.S.)

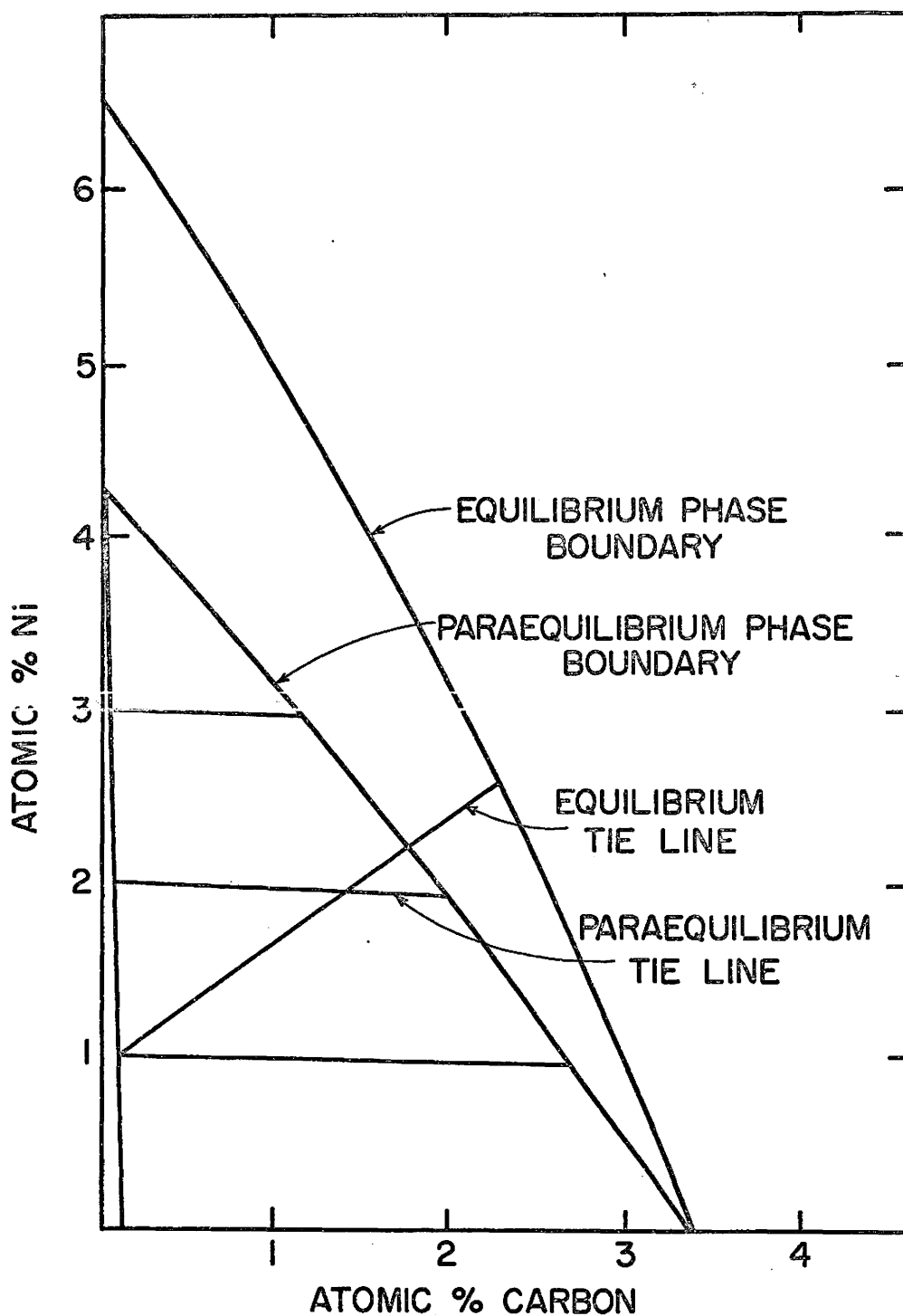


Figure VI. Representation of the paraequilibrium diagram for Fe-C-Ni alloys at 400° C. Also shown is the true equilibrium diagram and one equilibrium tie line.

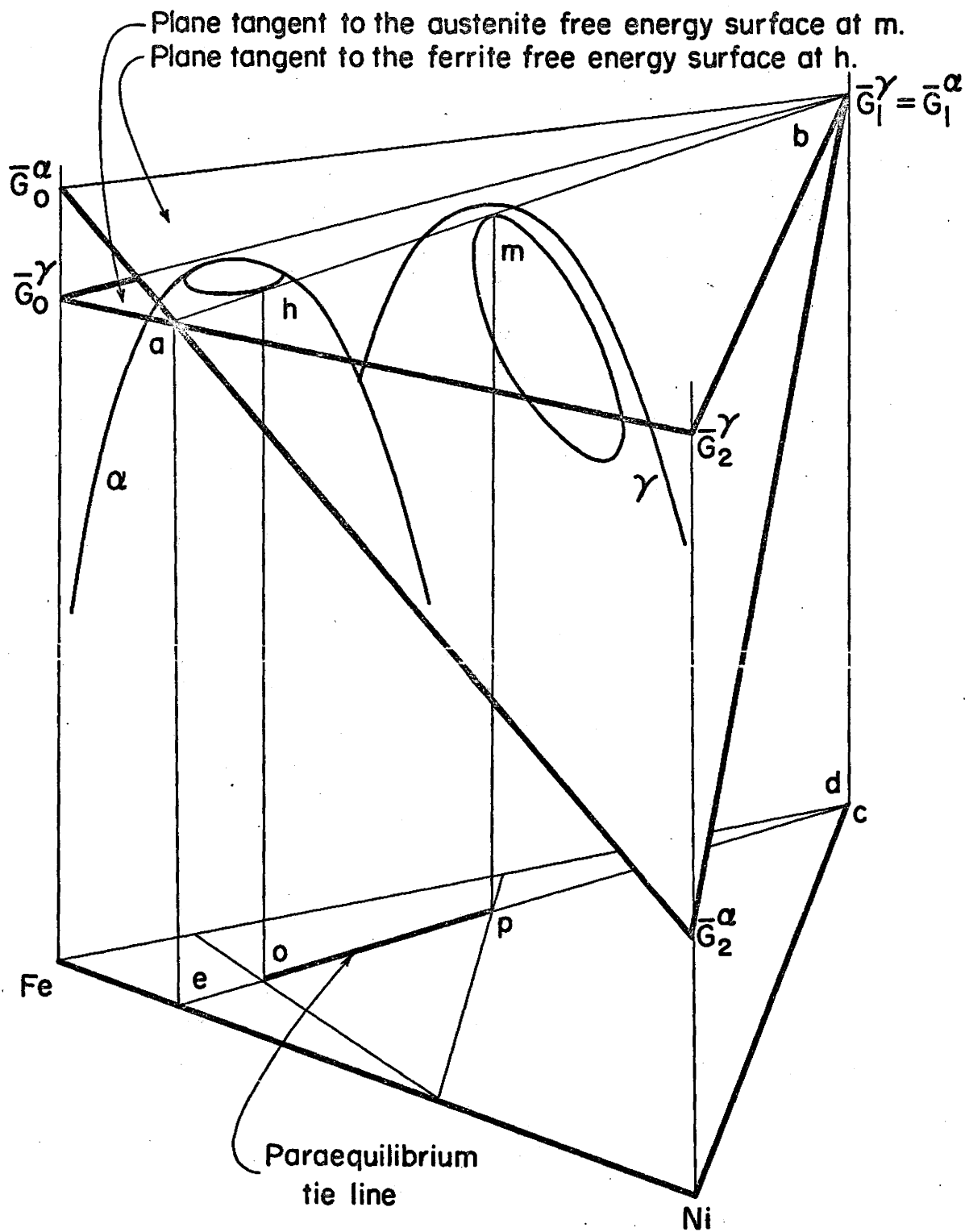


Figure VII. Schematic free energy surfaces for ferrite and austenite illustrating the paraequilibrium conditions.

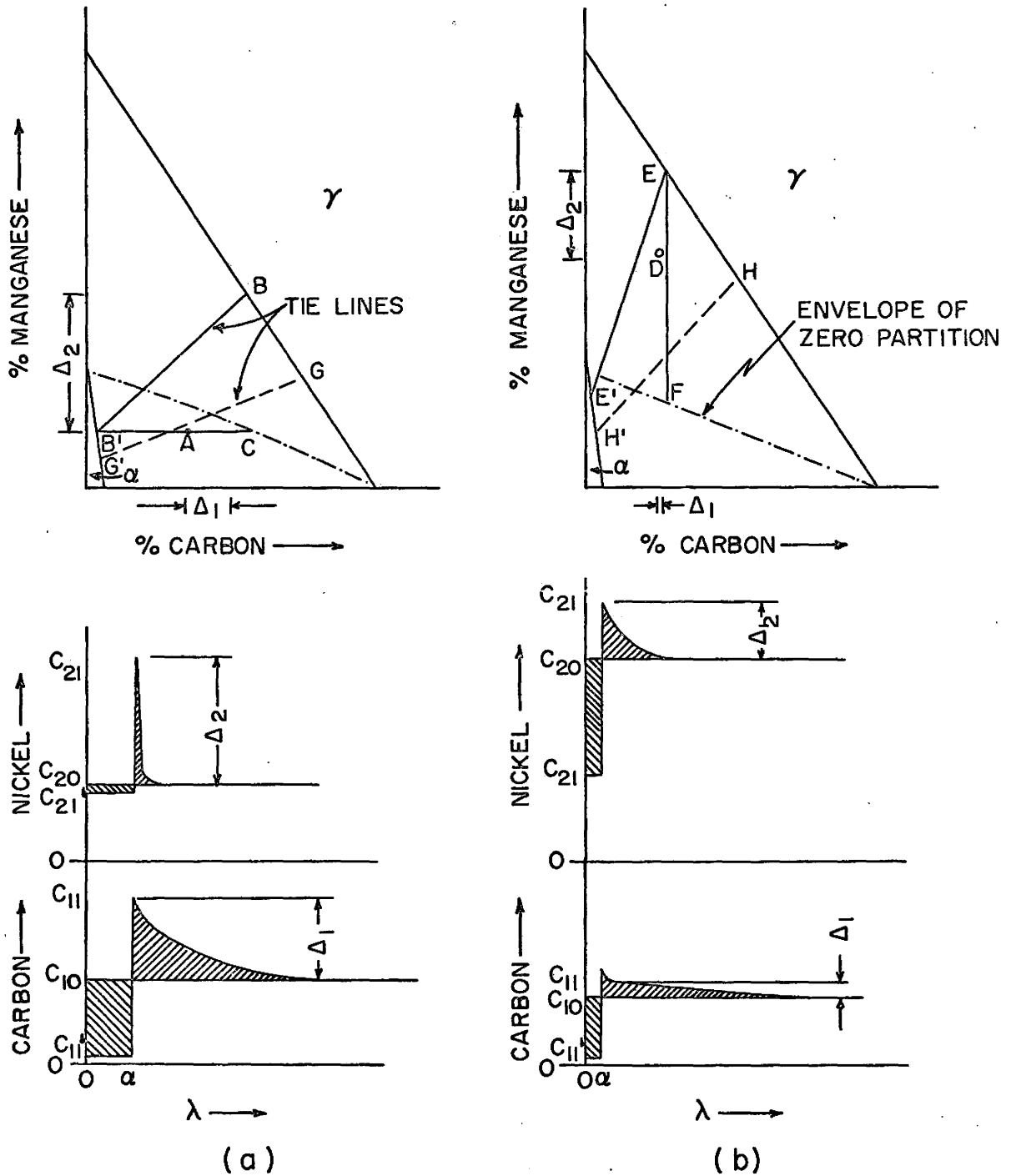


Figure VIII (a) Schematic penetration curves in γ space

(b) for ferrite growth in Fe-C-Ni austenites showing the effect of the envelope of zero partition on nickel distribution.

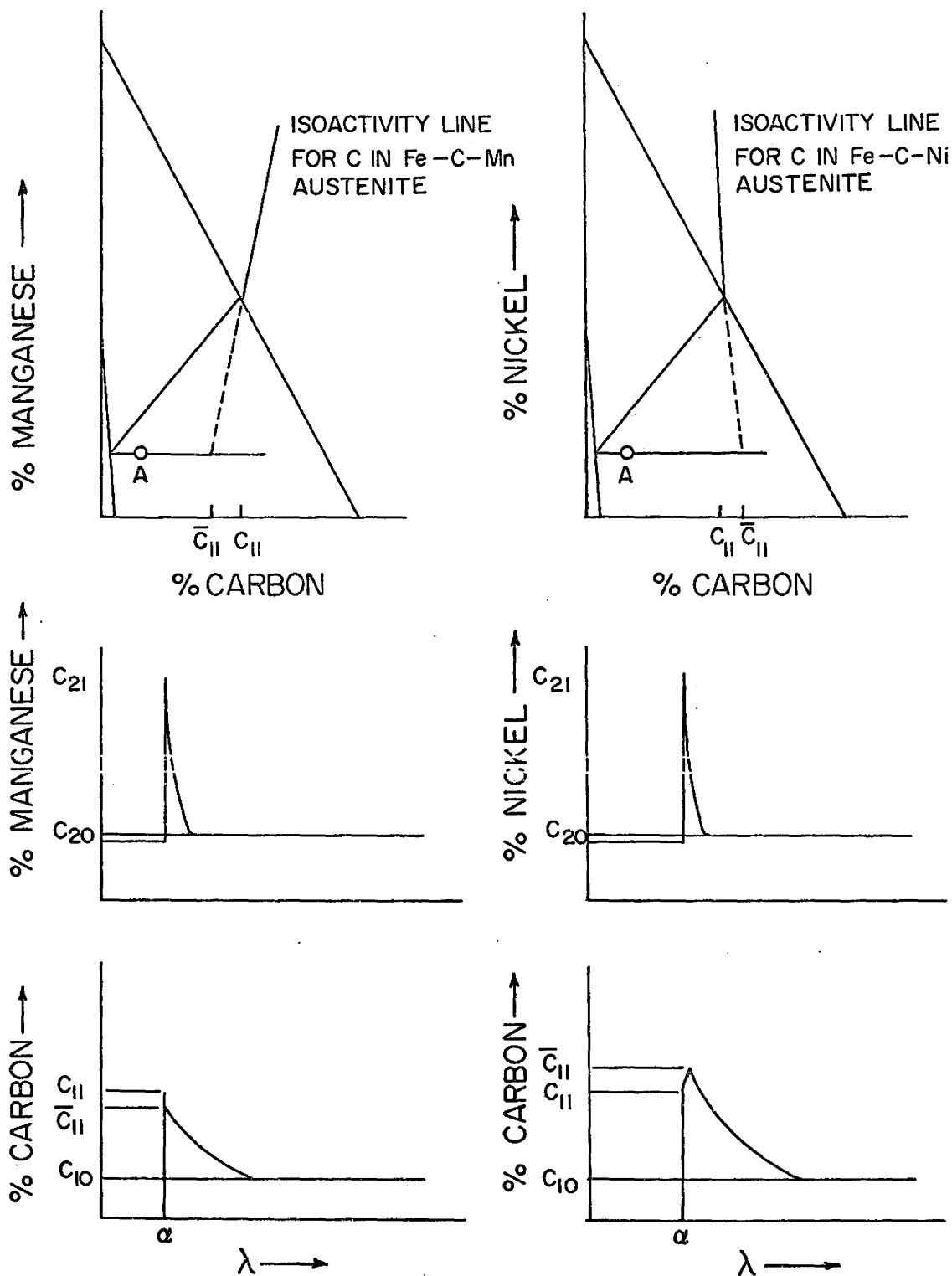


Figure IX. Representation of the difference between the effect of manganese and nickel through thermodynamic interaction on the formation of ferrite from supercooled austenite assuming local equilibrium.

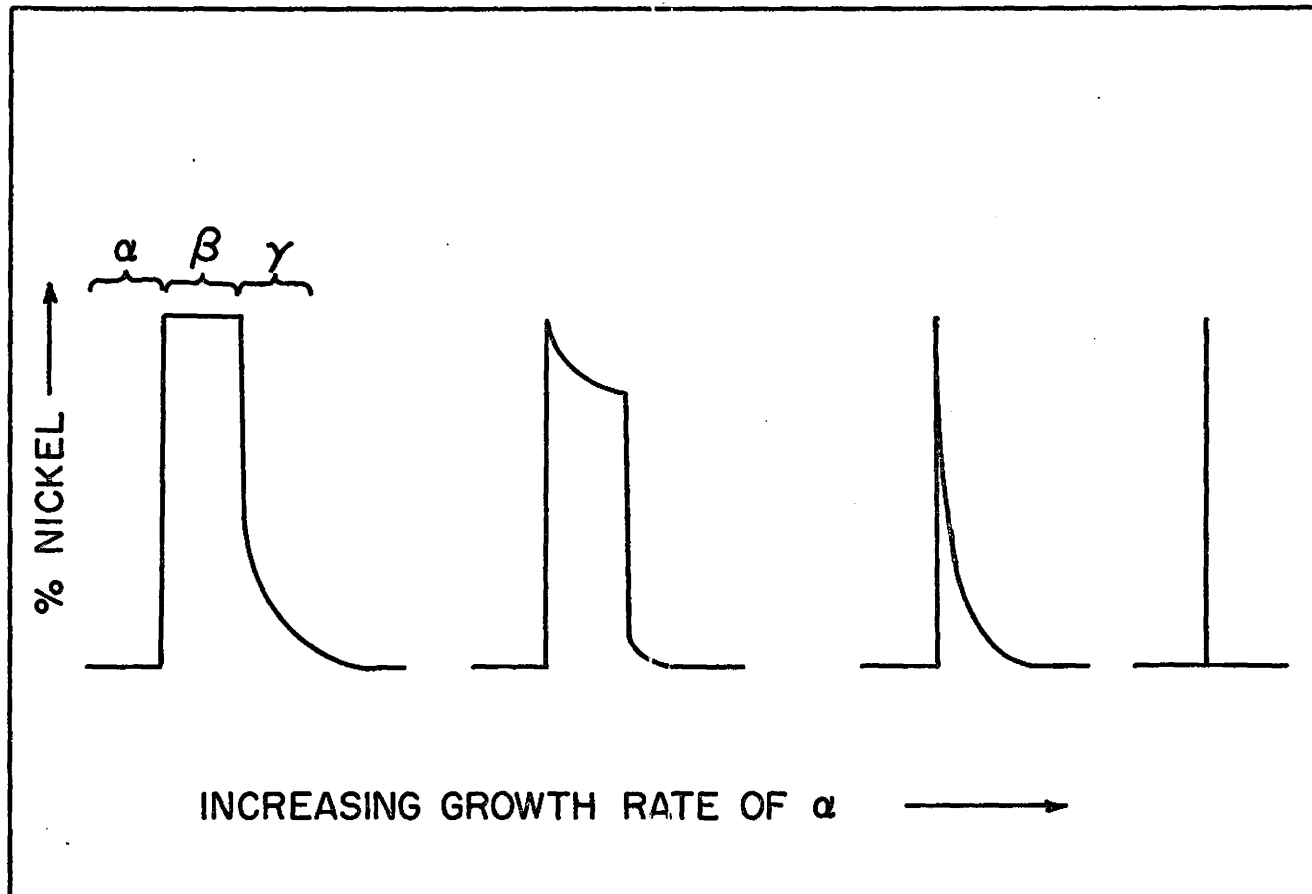


Figure X. Ni concentration profile inside and ahead of α/γ interface showing arbitrary boundary width.

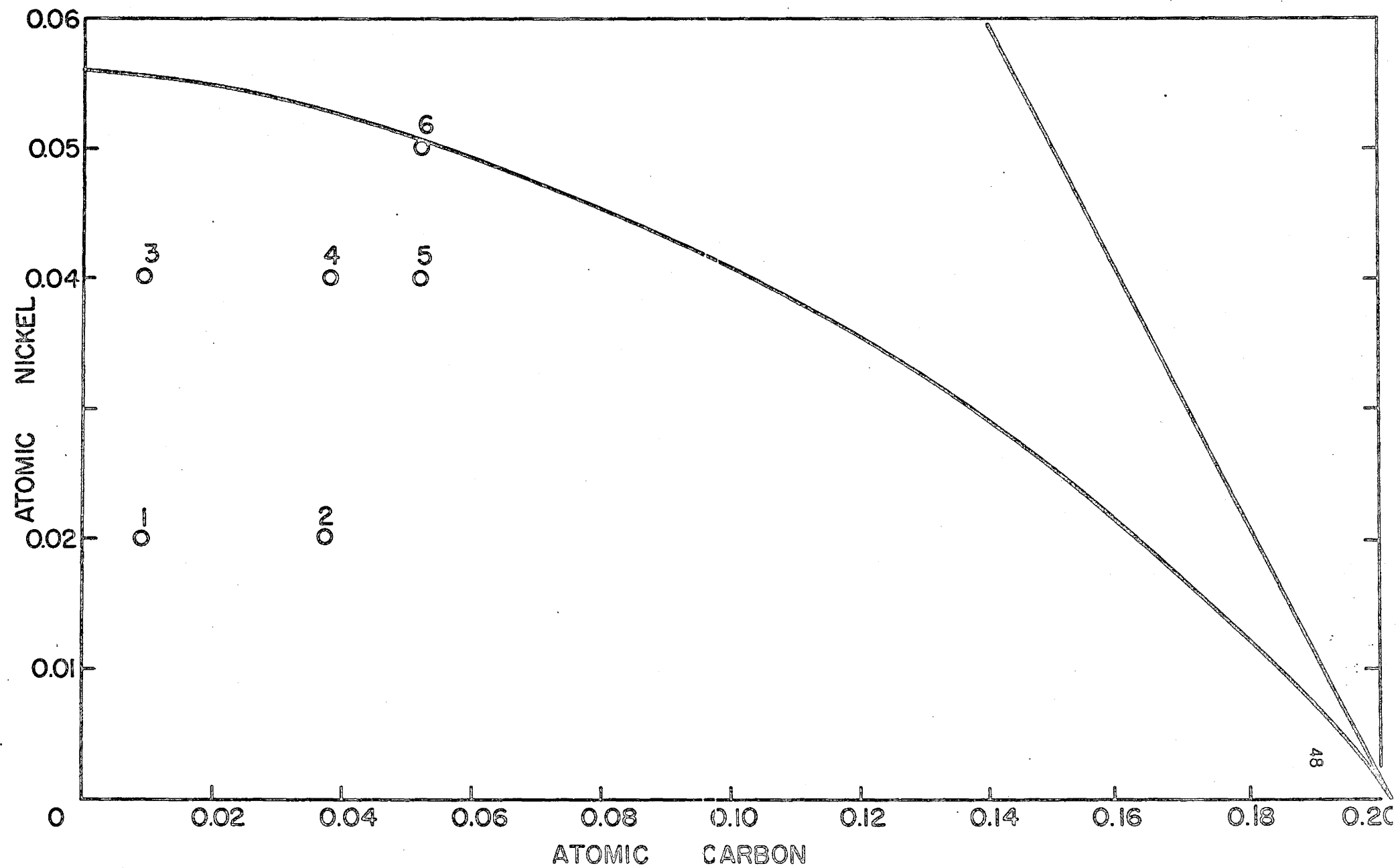


Figure XI. Calculated Fe-rich corner of Fe-C-Ni ternary isotherm (400°C).

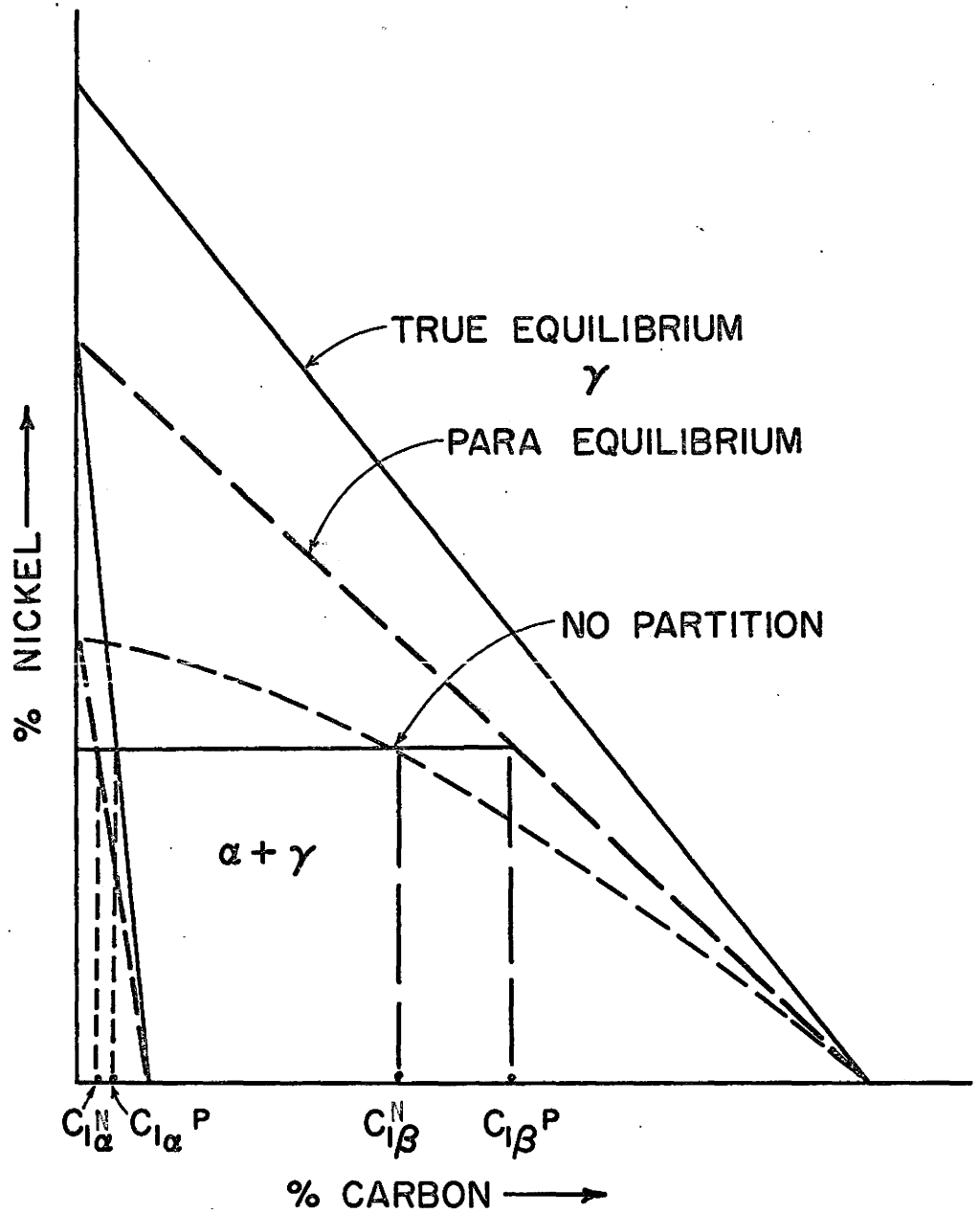


Figure XII. Schematic representation of iron-rich corner of Fe-C-Ni isotherm @ 4000 C.

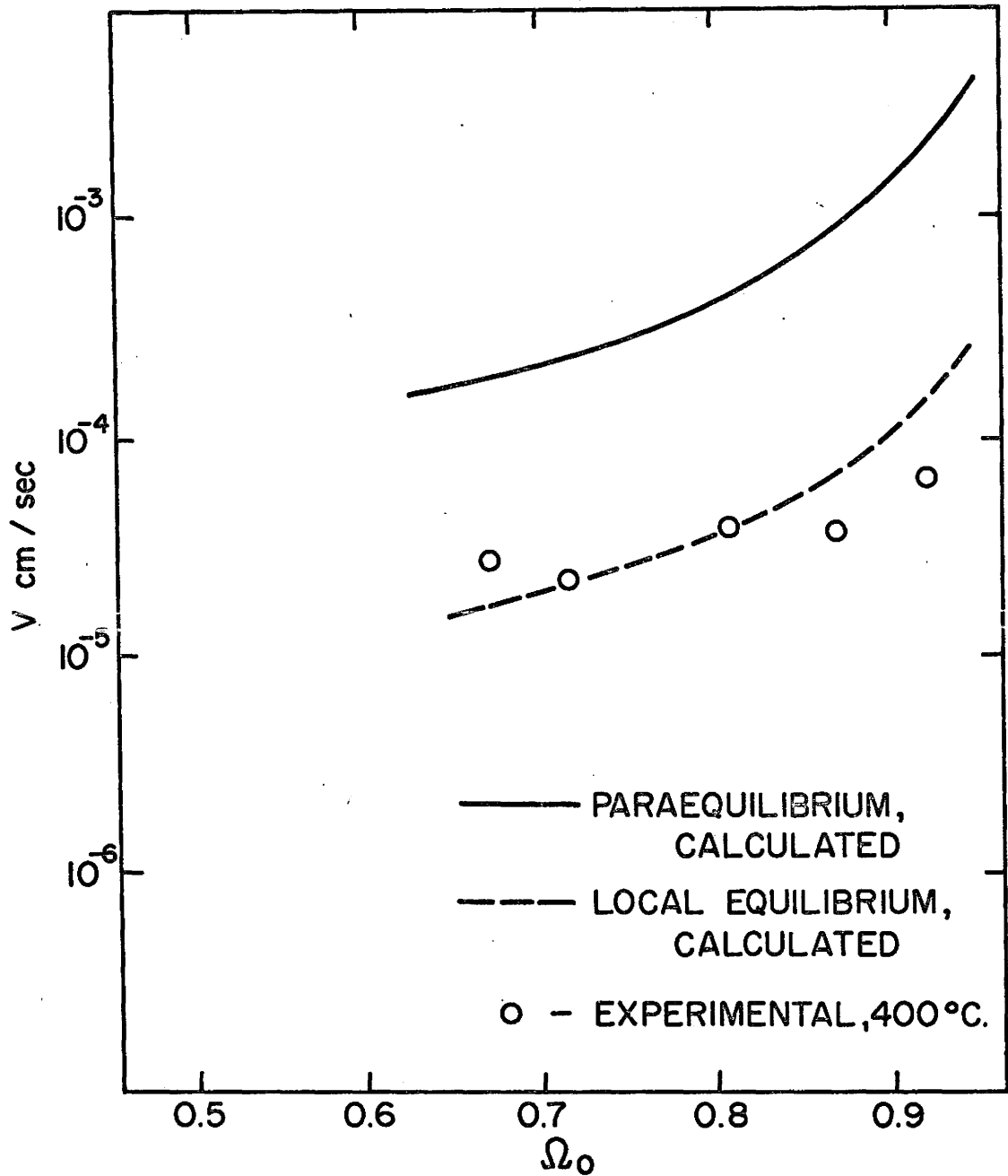
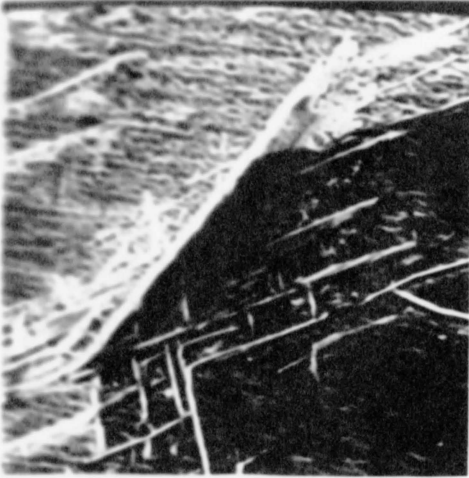
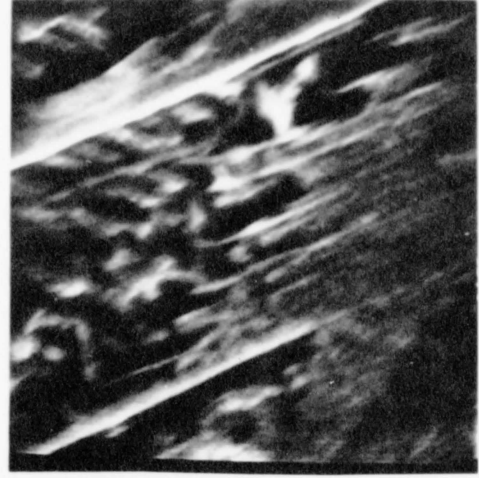


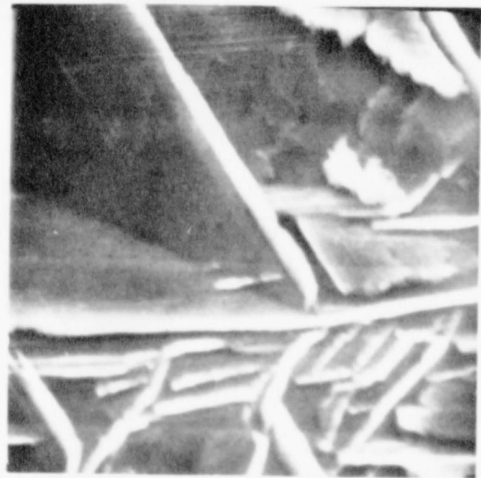
Figure XIII. Comparison of calculated local equilibrium no partition and paraequilibrium growth rates with experimental values.

I 1. α plate plane view.

I 2. Same plate view of sideways growth.



I 3. Same plate view of faceting.

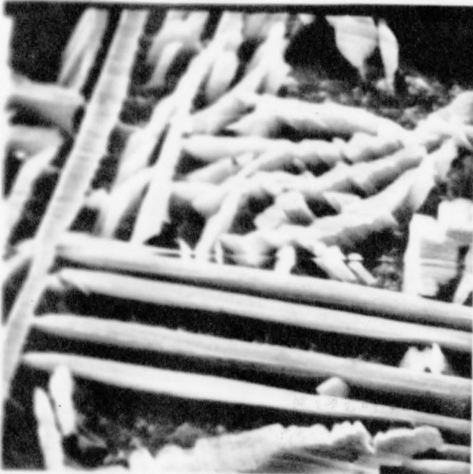
I 4. Two α plates plane view.I 5. Tip of thin α plate.I 6. Tip of thin α plates - 3 faces.



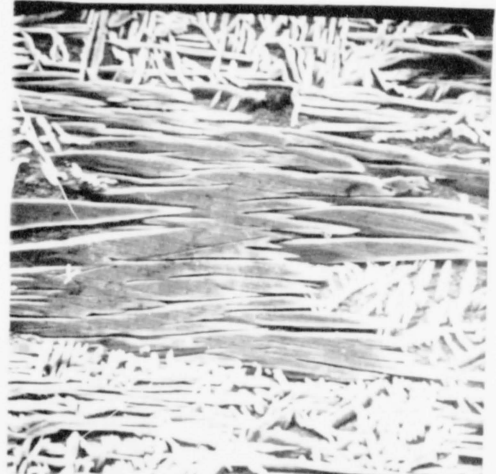
I 7. Group of coarsely faceted α precipitates.



I 8. Closeup of same precipitates.



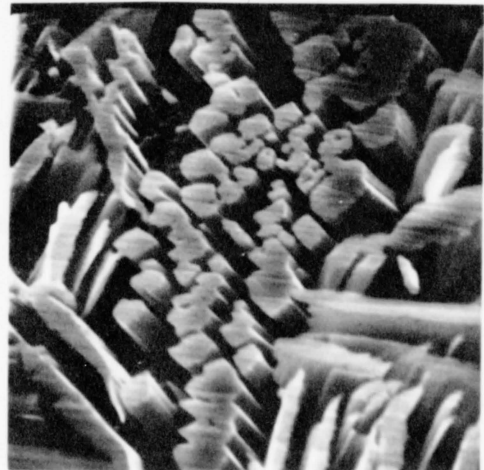
I 9. Orientation relationship of α precipitates.



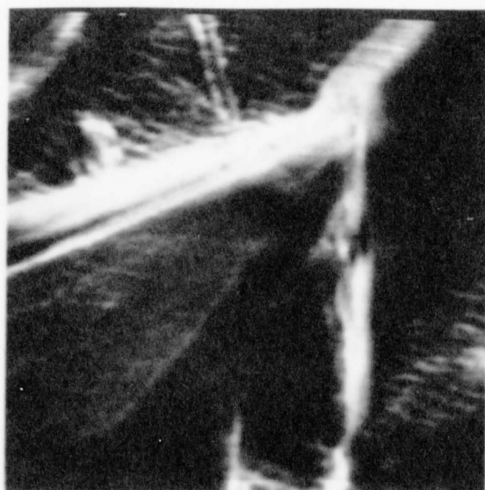
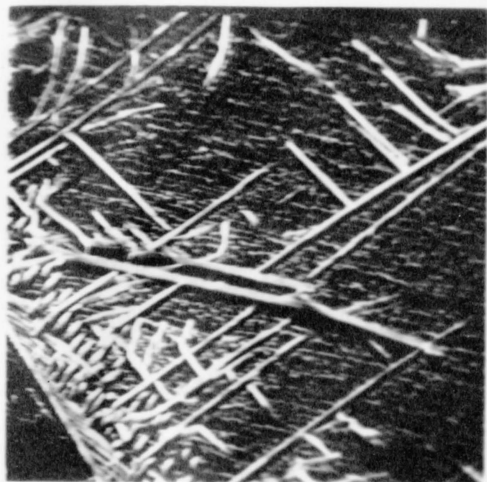
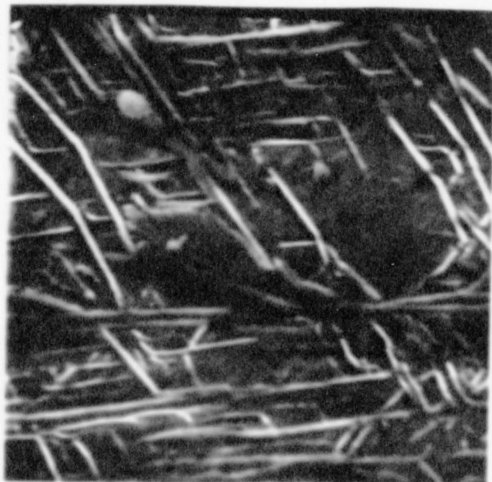
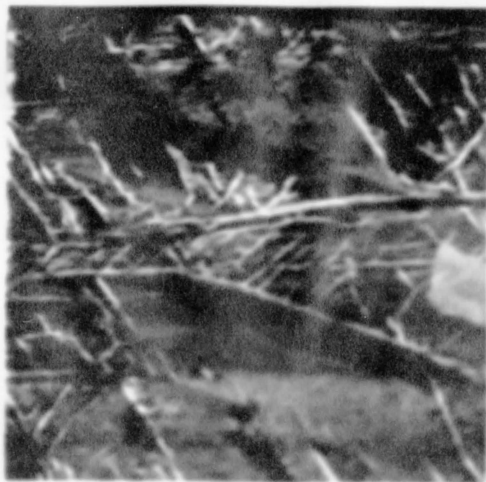
I 10. Plane view of sheave of α needles.

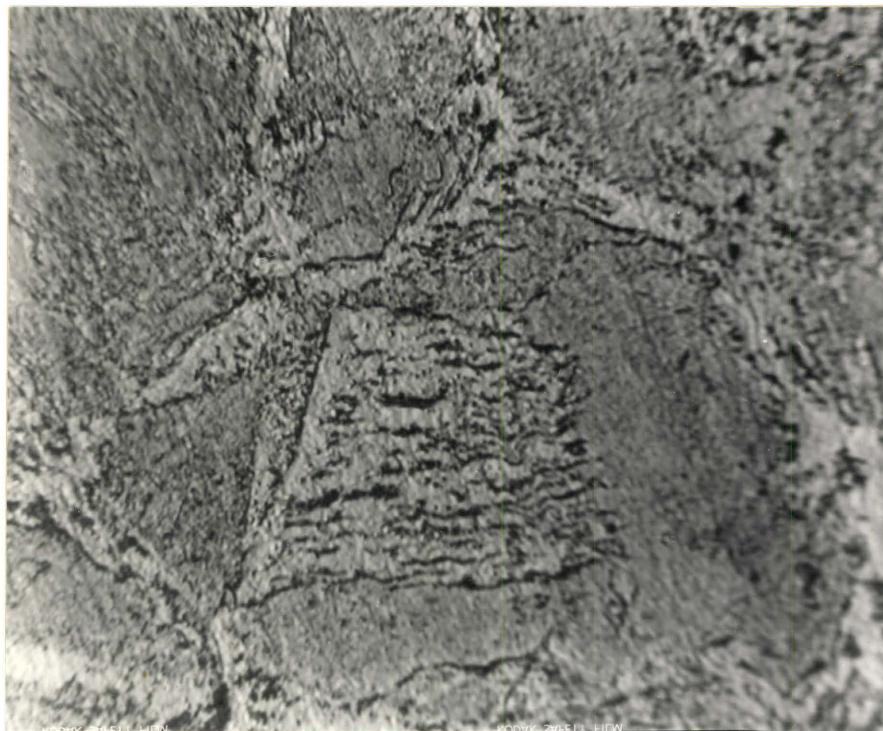


I 11. Closeup of tip from same sheave.

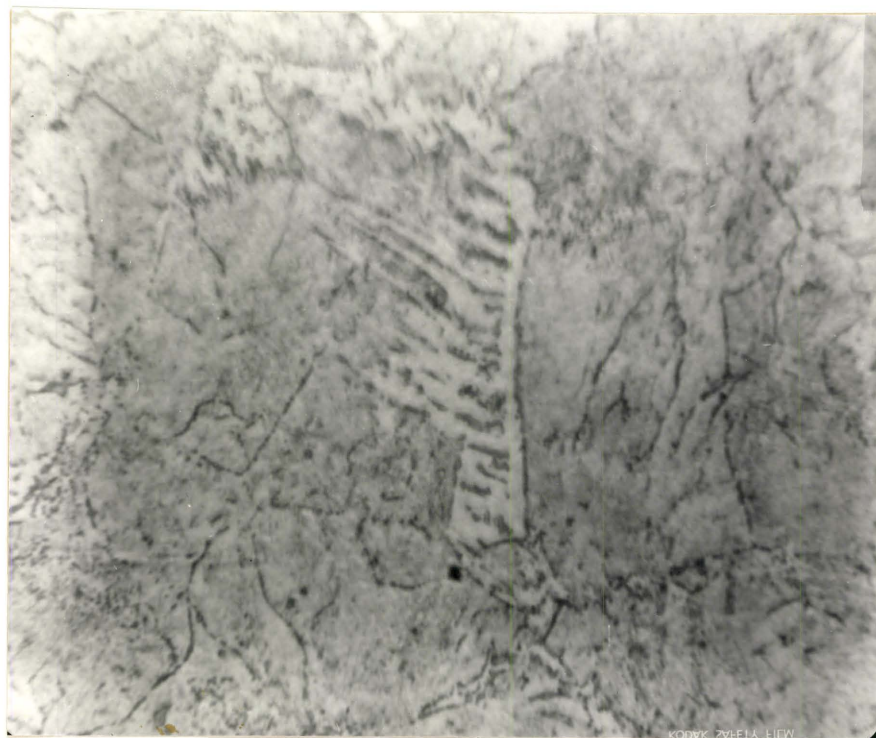


I 12. Cross-section of sheave of needles.

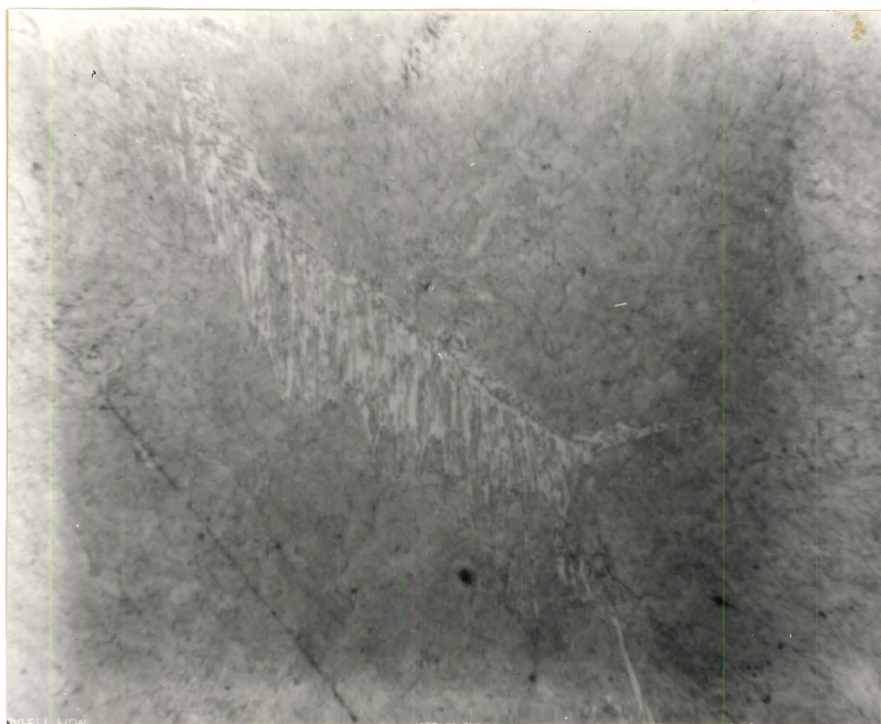
I 13. Face of α plate showing midrib.I 14. Opposite face of similar α plate.I 15. General group of α precipitates including grain boundary.I 16. Group of α plates.I 17. Group of α plates.



J I Fe - .8% C 2% Ni



J II Fe - .2% C 2% Ni



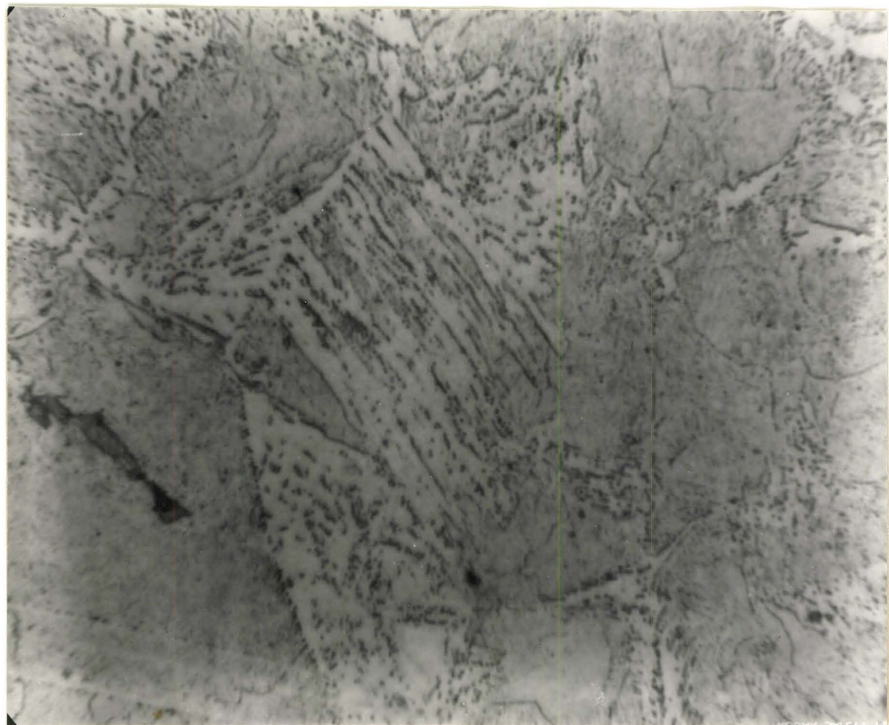
J III Fe - 1% C 5% Ni



J IV Fe - 1% C 4% Ni



J V Fe - .2% C 4% Ni



J Vi Fe - .8% C 4% Ni

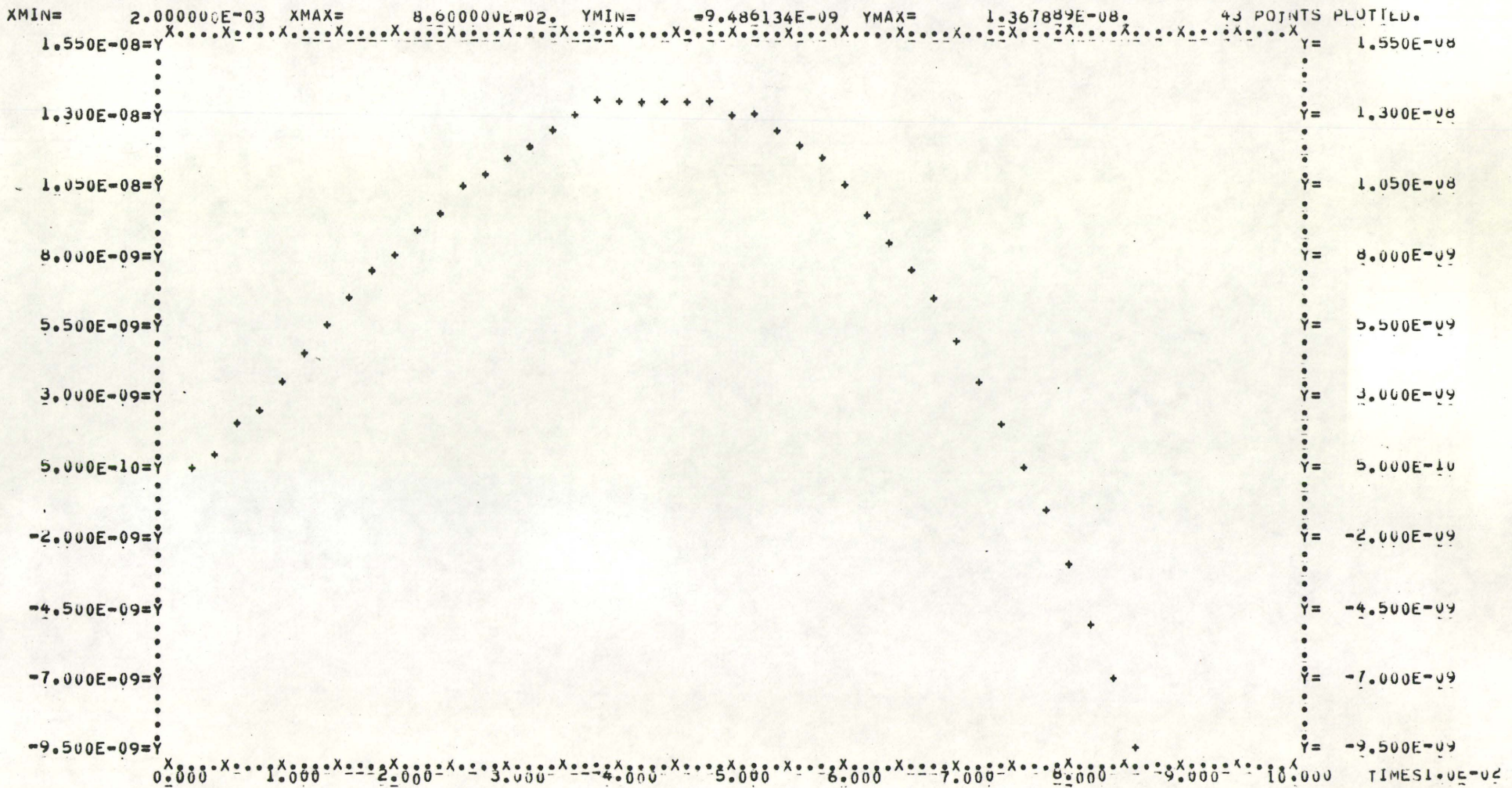


Figure XIV. Velocity (cm/sec) vs peclet number for plates at 250° C, Cu 42.5% Zn.

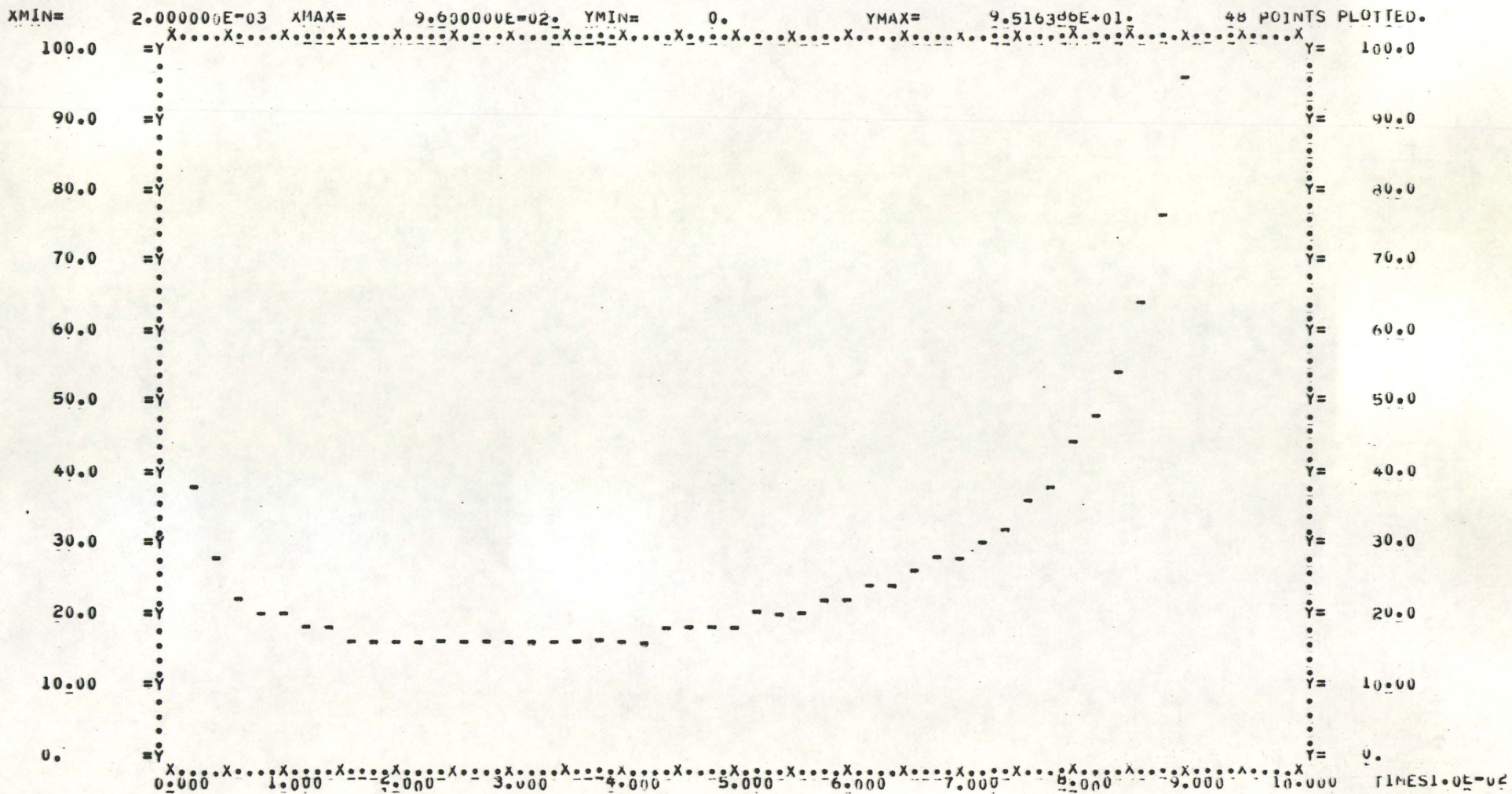


Figure XV. Critical radius ratio vs peclet number for plates at 250⁰ C, Cu 42.5% Zn.